University of Twente

EEMCS / Electrical Engineering
Control Engineering

Power-port modelling of an in-plane 3 DOF parallel micro-manipulator with feed-forward position control

Tijs Lammertink

M.Sc. Thesis

Supervisors
prof.ir. H.J.M.R. Soemers
prof.dr.ir. S. Stramigioli
ir. B.R. de Jong
dr.ir. G.J.M. Krijnen

December 2005

Report nr. 044CE2005
Control Engineering
EE-Math-CS
University of Twente
P.O. Box 217
7500 AE Enschede
The Netherlands

Summary

As part of the Multi Axis MicroStage project (MAMS), a 20-sim model of a 3 DOF parallel micro-manipulator was created. The model serves as a design tool and as verification in order to understand the behaviour of the actual system. The micro-manipulator was fabricated with MEMS technology. One of the possible applications for the manipulator is manipulation of samples in a Transmission Electron Microscope (TEM).

A multibody model of the manipulator was created with 20-sim's 3D Mechanics Editor. The multibody model contains the rigid bodies (with their positions, masses and inertias), and the kinematic construction of joints and rigid bodies. An equation submodel of the multibody model is exported to 20-sim. The compliant behaviour of the manipulator is added in 20-sim. Stiffness, masses and inertias were estimated on the basis of the physical dimensions of the actual device. The damping has been estimated roughly from measurements and is very low, which is typical for MEMS devices.

The manipulator is actuated by comb-drives. Since it is not trivial what voltage to apply to which comb-drive for movement of the manipulator's end-effector in a specific direction, a feed-forward position control was designed, which controls the manipulator in the desired coordinates.

Measurements on the real manipulator were performed: The platform deflection was measured for different comb-drive voltages as well as the resonance frequencies. The model was validated with measurements, which shows very similar relations between simulated and measured platform deflection as a function of the comb-drive voltages. The difference between simulations and measurements are: 2.3 % in x-direction, 3.9 % in y-direction and 12.8 % in φ-rotation. The simulated and measured resonance frequencies of the manipulator are also very similar: 7.1 % deviation in rotational resonance frequency, and 3.3 % and 3.1 % for the resonance frequencies in x and y-direction.

Contents

Chapter 1

Introduction

1.1 MAMS Project

This master assignment is part of the Multi-Axis MicroStage project (MAMS). The goal of the MAMS project is design and fabrication of a micro-manipulator with six degrees of freedom (DOF). The most important specifications the manipulator needs to achieve are:

- An enormously high positioning resolution; in the order of 1 nanometre
- Extremely small dimensions; in the order of 1 millimetre
- A very low drift; in the order of 0.1 nanometre per minute

Micro Electro Mechanical Systems (MEMS) process technology is used to fabricate the manipulator. It is a way to create mechanical structures on a silicon chip. MEMS technology is photo lithography based, which is also used in the electrical chip technology.

One of the applications for the micro-manipulator is manipulation of samples in a Transmission Electron Microscope (TEM). The small size of a MEMS device can be beneficial with respect to the conventional manipulator. It enables a larger tilt angle in the gap separating the magnetic lens poles; increasing achievable magnification combined with a large tilt angle. A small device obtains thermal equilibrium much faster. Thermal drift, in occurrence of temperature changes, stabilises quicker. Furthermore, the eigenfrequencies of a small device are very high. Firmly connected to the TEM column, the manipulator will nicely follow the movements of the electron beam due to vibrations of the TEM.

As part of the study on a 6 DOF manipulator, a parallel in-plane manipulator with 3 DOF is fabricated. It enables in-plane translation (along x and y) and in-plane rotation (about z). Together with an out-of-plane manipulator, which enables out-of-plane movements (translation along z and rotation about x and y), 6 DOF movements are possible.

1.2 Goal of the assignment

The goal of this assignment was to create a dynamic model of an in-plane 3 DOF parallel manipulator in 20-sim. The manipulator consists of three actuators, connected in parallel to an end-effector through flexures. Actuation is based on electrostatic attraction in a so-called comb-drive in pull-pull configuration. The end-effector is a platform that is controlled in the translational (along x and y) and rotational coordinates (about z). The model serves as a design tool and as verification in order to understand the actual system's behaviour. Special attention is paid to power-port modelling of the three flexures that suspend the end-effector in the manipulator.

A multibody model of the manipulator will be created in 20-sim's 3D Mechanics Editor. The equation submodel of the multibody model can be exported to 20-sim. In 20-sim, actuators, springs and dampers can be attached to the joints. Measurements should validate the model.

Since it is not trivial what voltage to apply to which comb-drive for movement of the platform in a specific direction, a feed-forward position control is to be designed, which computes the comb-drive deflection and actuation voltage as a function of the desired platform coordinates.

1.3 Report outline

Prior to the modelling, a conceptual analysis of both manipulators (in-plane and out-of-plane), concerning identification of rigid bodies and flexures is made in Chapter 2. The model of the leaf spring is treated in Chapter 3. In Chapter 4, a multibody model is created with 20-sim's '3D Mechanics Editor', also known as the 'body-editor'. And the equation submodel resulting from the body-editor and the bond graph model are discussed. In Chapter 5 a feed-forward position control that controls the platform in the desired coordinates is created and simulated. The model is validated with measurements in Chapter 6. The report is concluded in Chapter 7.

Chapter 2

Manipulation concepts

In this chapter, two manipulation concepts of a 6 DOF manipulator are explained (see also [5]). In Paragraph 2.1, a conceptual analysis of both manipulators is made. The identification of rigid bodies and flexures is treated in Paragraph 2.2.

2.1 Two manipulation concepts

Figure 2.1 shows two manipulation concepts: the in-plane 3 DOF parallel manipulator can be ‘stacked’ on top of the out-of-plane 3 DOF parallel manipulator, or it can be done the other way around. The in-plane manipulator enables translation along x and y and rotation about z. The out-of-plane manipulator enables rotation about x and y and translation along z. This series connection of both 3 DOF manipulators results in a 6 DOF manipulator.

The concept from figure 2.1(a) enables in-plane movement of the bottom platform and out-of-plane movement of the top platform. The bottom platform is connected to three ‘arms’ at its corners. Each arm is connected to the fixed world. The translational actuators exert forces on the platform through joints. In the figure, the joints are represented by circles, but in reality flexures transfer forces to the platform. The top platform is also connected to three arms on its corners. The arms are fixed to the bottom platform through joints. Translational actuators exert forces on the platform through joints.

The concept of figure 2.1(b) enables out-of-plane movement for the outer platform and in-plane movement of the inner platform.

2.2 Analysis of the in-plane manipulator

Figure 2.2 shows a photo of the in-plane manipulator through an optical microscope. The outer dimensions are $4.5 \times 5.2\,\mathrm{mm}$ and the design has a 120° point-symmetry. In the centre, the end-effector (platform) is located. Reinforced flexures connect the platform to so-called shuttles. Each shuttle is suspended by four folded flexures and actuated by two comb-drives in pull-pull configuration.

Only flexible (or elastic) suspensions are used. This has the advantage of a more accurate displacement, because regular non-elastic suspensions, constructed from bearings and joints like hinges, pivots or sliders have play and suffer from stick-slip. With the current MEMS technology, the minimum achievable play is much bigger than the specified positioning resolution. The disadvantage of using elastic suspensions is that it introduces stiffness. A force is necessary not only to put the platform in a certain position, but also to keep it there. Another disadvantage is that for flexible suspensions the maximum deflection and bending is limited, compared with non-elastic joints of the same size. Hence, flexible suspensions are bigger in general.

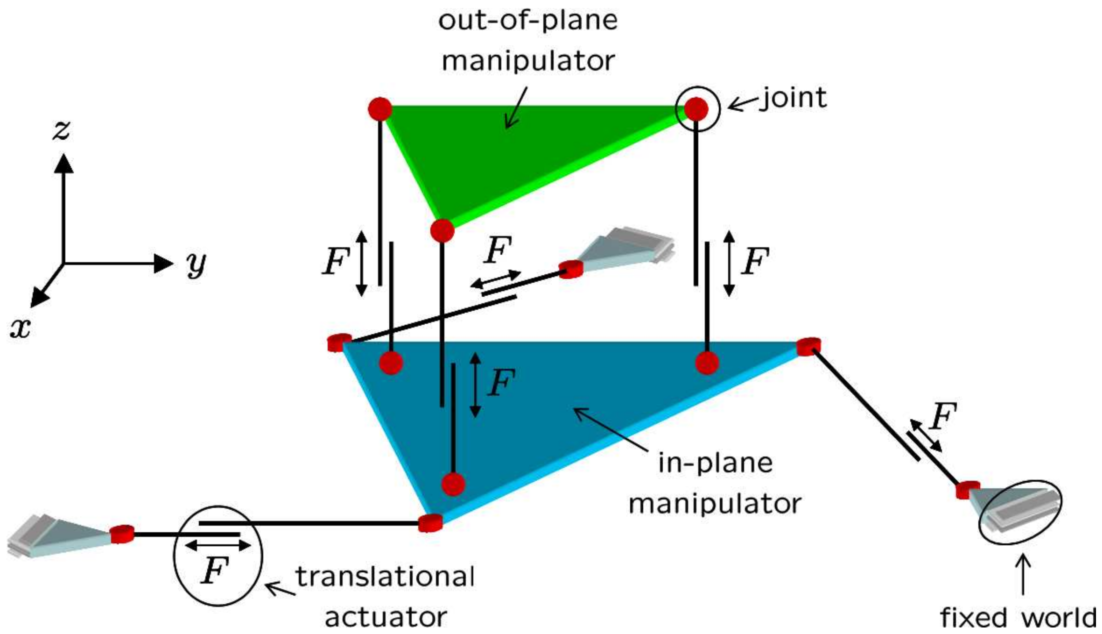

(a) Out-of-plane manipulator 'stacked' on in-plane manipulator. Out-of-plane manipulator is constrained for in-plane movements (= translation along x and y and rotation about z) and in-plane manipulator is constrained for out-of-plane movements (= translation along z and rotation about x and y)

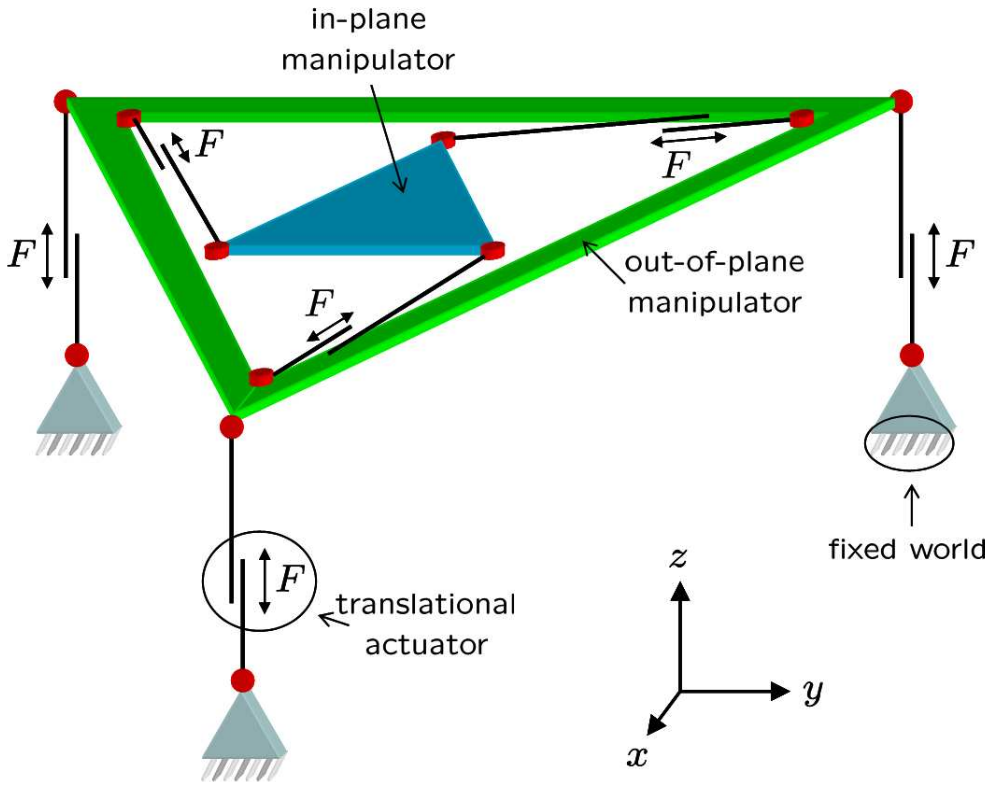

(b) In-plane manipulator 'stacked' on in-plane manipulator. Out-of-plane manipulator is constrained for in-plane movements (= translation along x and y and rotation about z) and in-plane manipulator is constrained for out-of-plane movements (= translation along z and rotation about x and y)

Figure 2.1: Manipulation concepts

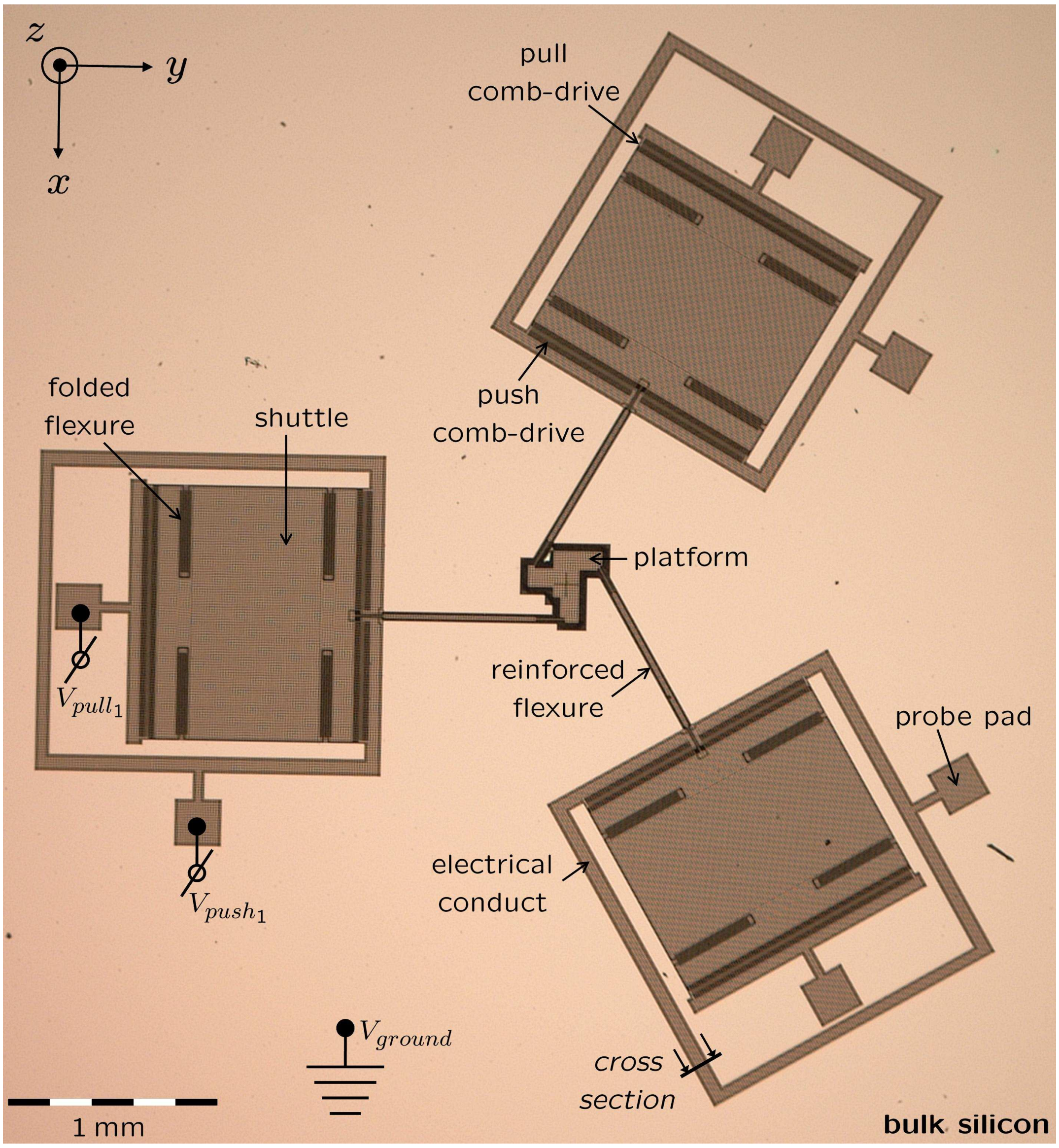

Figure 2.2: Photo of the in-plane manipulator through an optical microscope

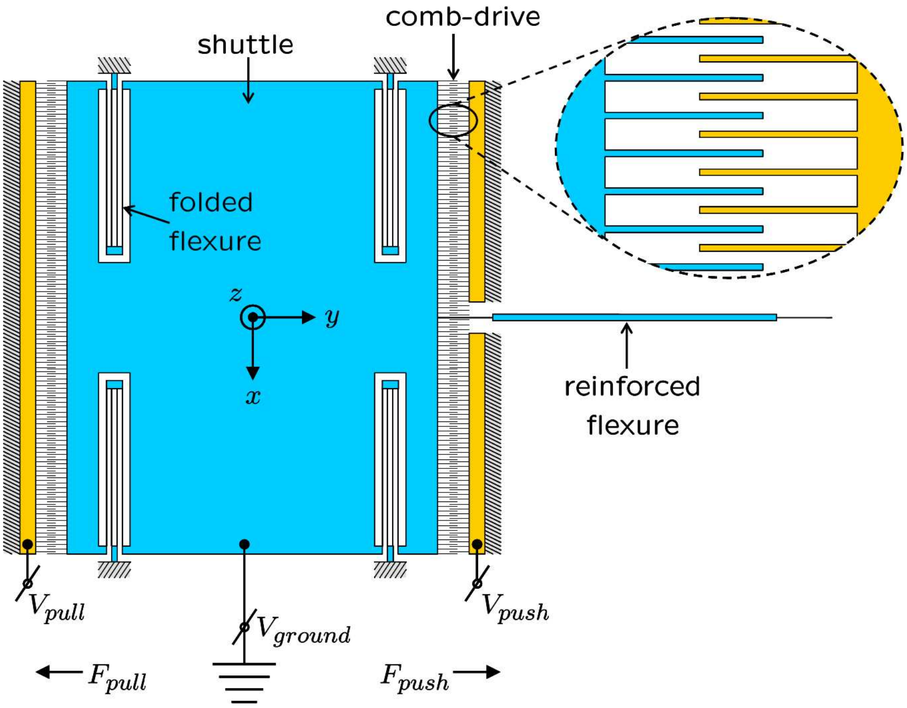

Figure 2.3: Schematic figure of an arm and a close-up of a comb-drive

Comb-drive

Figure 2.3 shows an on-scale schematic figure (scale 52:1) of one 'arm' and a close-up of a comb-drive (scale 420:1). The arm consists of a shuttle, two comb-drives, four folded flexures and a reinforced flexure. A comb-drive is a linear motor that consists of a movable and a stationary set of comb-fingers. When a voltage is applied to the comb-drive, an electrostatic force is generated, and as a result the comb fingers attract each other in the y-direction. The electrostatic forces between the fingers in x-direction compensate each other. The comb-drive deflection depends on the stiffness of the folded flexures and the reinforced flexures. The relation between force and voltage is quadratic:

$$F_{comb} = \frac{n\epsilon h}{g} V_{comb}^2 \tag{2.1}$$

With n the number of fingers, ϵ the dielectric constant of the medium between the fingers, which is air or vacuum, h the height of the comb-fingers and g the gap between the fingers.

A comb-drive can only generate a force in one direction, since it can only attract its fingers (two opposite charges always attract each other). Therefore, the comb-drives on each shuttle are configured in pull-pull configuration to enable movement in positive as well as negative direction. One comb-drive pulls at one side of a shuttle and the other comb-drive pulls at the other side. However, the comb-drives that 'push' the platform are called push comb-drives, and the comb-drives that 'pull' the platform are called pull comb-drives, to distinguish between them. The force due to both comb-drives is calculated as follows:

$$\begin{cases} F_{push} = \dfrac{n\epsilon h}{g} V_{push}^2 \\ F_{pull} = \dfrac{n\epsilon h}{g} V_{pull}^2 \\ F_{pull} = -F_{push} \end{cases} \Rightarrow \quad F_{push} = \frac{n\epsilon h}{g}\left(V_{push}^2 - V_{pull}^2\right) \tag{2.2}$$

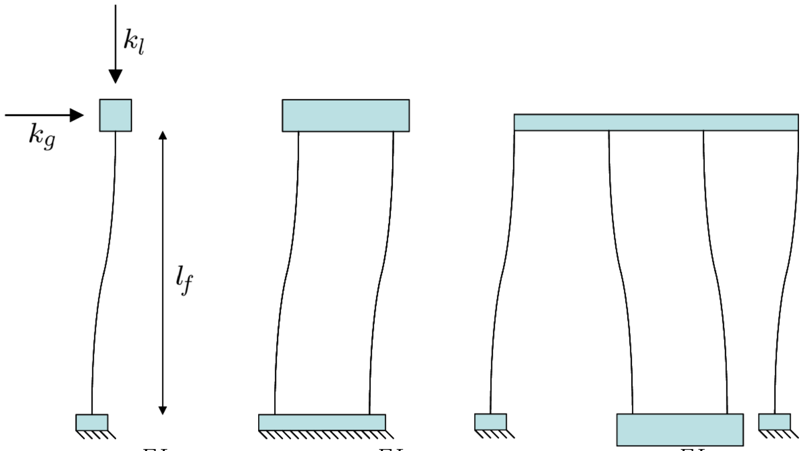

(a) $k_g = 12\frac{EI}{l_f^3}$ (b) $k_g = 24\frac{EI}{l_f^3}$ (c) $k_g = 12\frac{EI}{l_f^3}$

Figure 2.4: Folded flexure

Folded flexures (comb-drive and shuttle suspension)

A folded flexure is an element with four combined flexures of length l_f to make it suitable for parallel guiding and constrain rotational movements. Moreover, the shortening effect in longitudinal direction has been compensated. Figure 2.4(a) shows one flexure; it has a guiding stiffness (k_g) of $12\frac{EI}{l_f^3}$, with I the area moment of inertia of the folded flexure, and E Young's modulus of silicon. Figure 2.4(b) shows two parallel flexures; together they have a guiding stiffness that is two times bigger than one flexure: $24\frac{EI}{l_f^3}$. A folded flexure (Figure 2.4(c)) is in fact a series construction of two times two parallel flexures. The outer two flexures, as well as the inner two flexures, are parallel to each other. The two inner flexures and two outer flexures are in series to each other. Hence the guiding stiffness of one folded flexure becomes two times smaller than that of two parallel flexures, so it has the same guiding stiffness as one flexure has: $12\frac{EI}{l_f^3}$. Each shuttle is suspended with four folded flexures in parallel, which have a combined guiding stiffness that is simply four times bigger: $48\frac{EI}{l_f^3}$.

The same story holds for the longitudinal stiffness (k_l). A folded flexure has the same longitudinal stiffness as one flexure: $\frac{EA}{l_f}$. The combined longitudinal stiffness of four folded flexures is again four times bigger: $4\frac{EA}{l_f}$.

Trench

Figure 2.5 shows a schematic top view and two schematic cross sections of a trench (the location is shown in Figure 2.2). Trenches separate different potentials and define regions serving as electrical connections to the comb-drives. The so-called twin-etching method requires that the shuttles and the platform contain square holes. The cross section shows that the trench isolation electrically isolates the trench from the ground potential V_{ground}. Mechanically, the trench is fixed to the bulk. The probe pad potential V_{push_2} is transferred to the stationary fingers of the comb-drive through the trench. The ground potential is transferred to the movable fingers of the comb-drive via the bulk, and through the folded flexures.

Assumptions

The folded flexures are assumed to be compliant in their guiding direction, which is the direction the comb-drive actuates. And they are assumed to be stiff in the other directions. This makes 1 DOF unconstrained

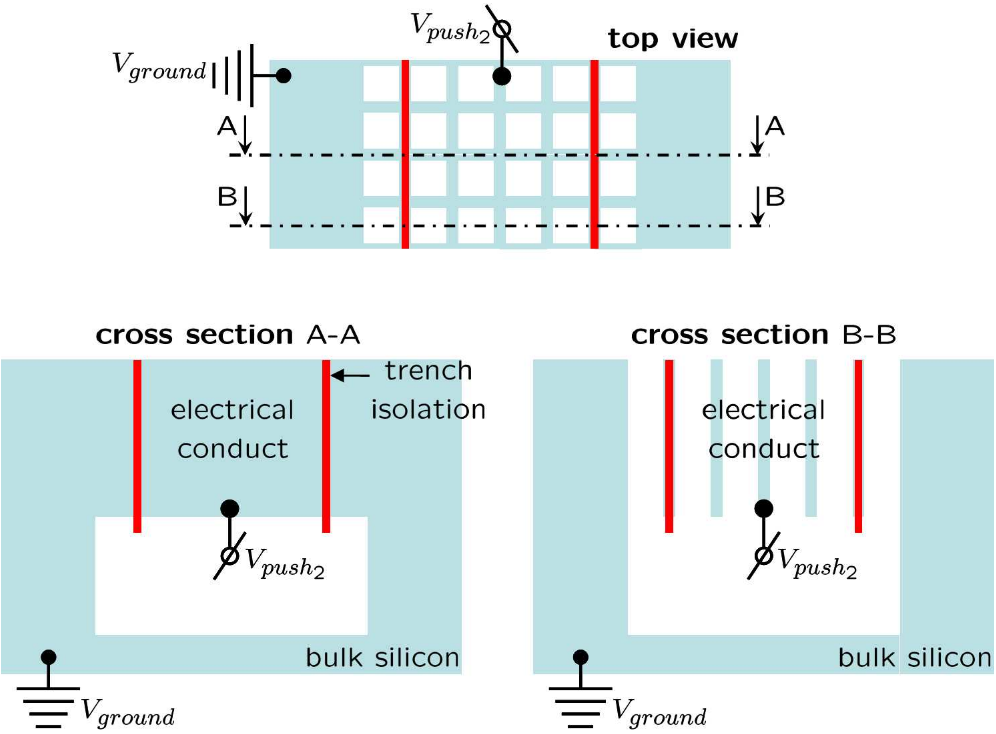

Figure 2.5: Schematic cross sections of a trench isolated region

and 5 DOF constrained. The longitudinal stiffness is in the order of 10^4 bigger than the guiding stiffness, so the folded flexures are assumed to be rigid in the longitudinal direction. The Rz rotational stiffness (see Figure 2.3) that the shuttle feels due to the four folded flexures is very big, because of the relatively large distance between two neighbouring folded flexures. The Rx and Ry tilt stiffness that the shuttle feels is also very big, because of the use of four folded flexures instead of one or two.

Usually, flexures allow torsional movements due to torsion stiffness. This is undesirable when only in-plane movements are actuated, as in this manipulator. But since the parallel construction of three flexures (that connect the platform to the shuttles) does not allow out-of-plane movements, torsion movements of the flexures are constrained. Hence, only the in-plane movements of the flexure are assumed to be compliant and a 3 DOF model of the flexure will be sufficient.

The shuttles and the platform are modelled as rigid bodies. The leaf springs and folded flexures have compliant behaviour and are modelled as springs. If the mass of the springs is much less than that of the shuttles and the platform, the mass of the springs may be neglected. And if the shuttles and platform are much stiffer than the springs, the shuttles and platform may be assumed rigid.

Chapter 3

Flexure model

In this chapter, the flexure model is addressed. Paragraph 3.1 shows that it is important to choose symmetric coordinates for the stiffness matrix of a 3 DOF flexure. In Paragraph 3.2 a 3 DOF flexure is constructed from 1D springs in 20-sim, and it will be shown that it is impossible to construct a symmetric leaf spring from 1D springs. In Paragraph 3.3 a solution is given to describe the stiffness matrix in symmetric coordinates, but still using an asymmetric joint-structure to construct the flexure. In Paragraph 3.4 the solution is validated by simulations. The manipulator has reinforced flexures which are treated in Paragraph 3.5.

3.1 Choosing symmetric stiffness matrix coordinates

Figures 3.1(a) and 3.1(b) show an undeformed flexure, which is clamped to the fixed world at the left side. At the right side, a rigid body is connected. A massless construction is connected to the bottom of the rigid body. The in-plane forces are applied on the centre of the spring. Usually a flexure is only constrained (to a certain extent) for translation along z and rotation about x. However, since the parallel construction of three flexures in the manipulator does not allow torsional movements, choice is made not to consider torsional stiffness about y. Hence, the flexure is assumed to be constrained in the out-of-plane directions (3 DOF) and unconstrained in the in-plane directions (3 DOF).

The flexure in Figures 3.1(a) is rotated around y with respect to the flexure in Figures 3.1(b). The stiffness matrix of the flexure, around equilibrium and for small deformations, reflected to a point at $y = \frac{1}{2}l$ (in its centre of stiffness (COS)) is derived in Appendix B.2:

$$K_c = \begin{bmatrix} \dfrac{EI}{l} & 0 & 0 \\ 0 & 12\dfrac{EI}{l^3} & 0 \\ 0 & 0 & \dfrac{EA}{l} \end{bmatrix} \tag{3.1}$$

The force-deflection relation for this flexure (for small deflections) is:

$$\begin{bmatrix} M \\ F_x \\ F_y \end{bmatrix} = K_c \begin{bmatrix} \varphi \\ x_c \\ y_c \end{bmatrix} \tag{3.2}$$

The energy function of this flexure (for small deflections) is quadratic:

$$E = \frac{1}{2} \begin{bmatrix} \varphi & x_c & y_c \end{bmatrix} K_c \begin{bmatrix} \varphi \\ x_c \\ y_c \end{bmatrix} = \tfrac{1}{2}\frac{EI}{l}\,\varphi_c^2 + 6\frac{EI}{l}\,x_c^2 + \tfrac{1}{2}\frac{EA}{l}\,y_c^2 \tag{3.3}$$

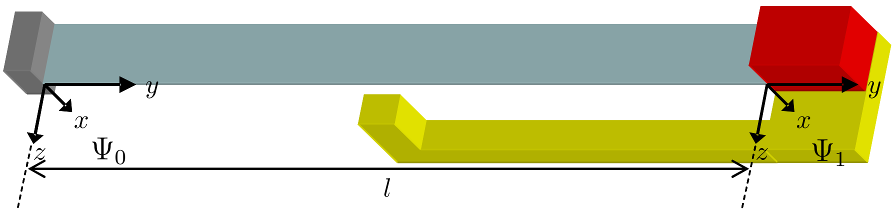

(a) Undeformed flexure (rotated about y with respect to flexures below)

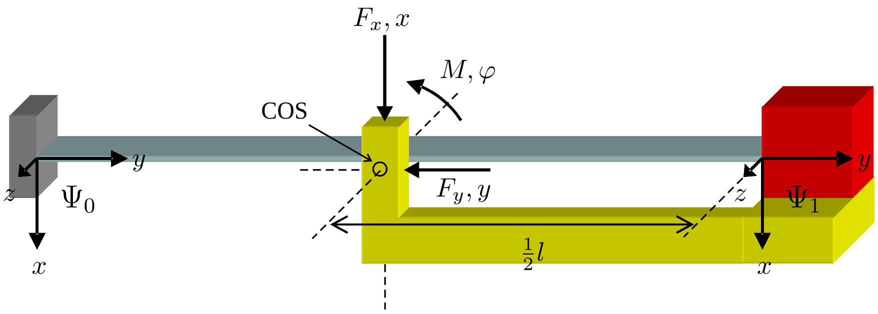

(b) Undeformed flexure

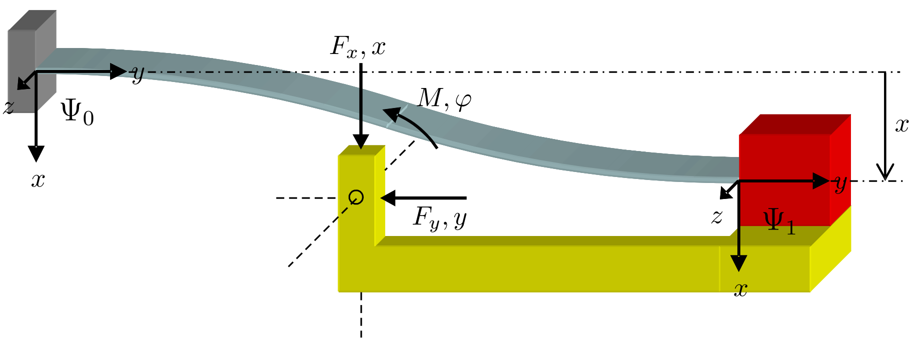

(c) Deformed flexure due to a positive force F_x (M and F_y are zero)

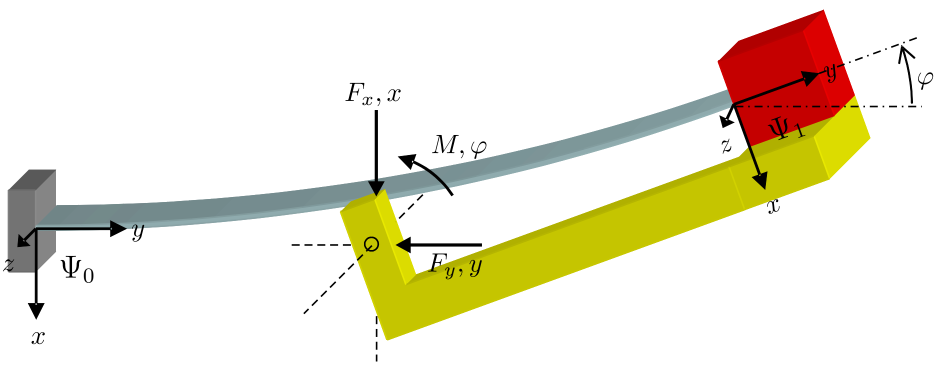

(d) Deformed due to a positive torque M (F_x and F_y are zero) in world orientation

Figure 3.1: Flexure

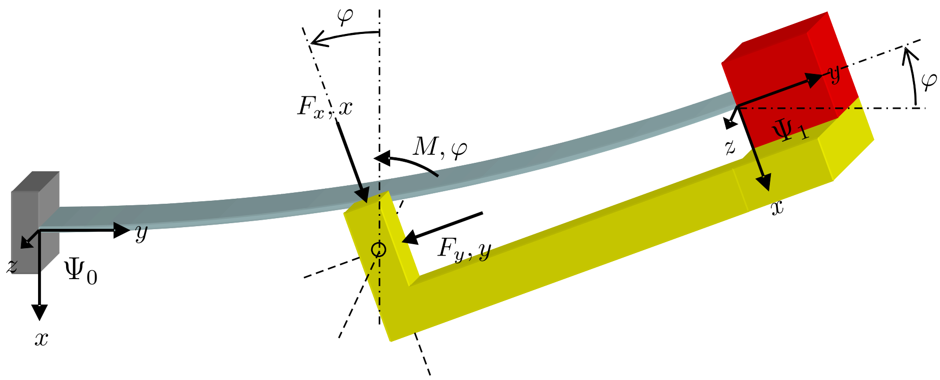

(e) Deformed due to a positive torque M (F_x and F_y are zero) in body orientation

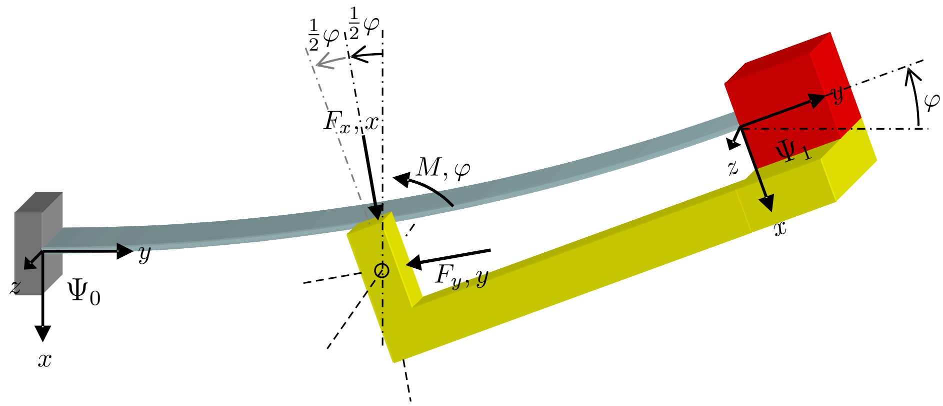

(f) Deformed due to a positive torque M (F_x and F_y are zero) with symmetric orientation

Figure 3.1: Flexure

Figure 3.1(c) shows the same flexure with a deformation due to a positive force in x-direction F_x, (M and F_y are zero). According to the symmetric stiffness matrix, only a deflection in x-direction results.

Figure 3.1(d) shows the flexure with a deformation due to a positive torque M, (F_x and F_y are zero). The only deformation is a rotation φ. The orientation of the forces and torque is chosen such, that it coincides with world coordinates (Ψ_0). A flexure is a symmetric element in reality, because it does not matter whether the left side of the flexure is clamped and the forces affect the right side, or the other way around; the deflection stays the same in both cases. However, the flexure is not modelled symmetrically with this choice of orientation of forces and torque, because it does matter whether the flexure is viewed from right to left or from left to right. Imagine that the two terminals of the spring are swapped, i.e.:

- Instead of the left side, the right side is clamped to the fixed world
- Instead of the right side, the mass is connected on the left side
- The flexure is turned around 180°

Then the flexure in Figure 3.1(e) results. But now, the coordinates are defined differently. In fact, the orientation of the forces is now chosen such, that it coincides with the coordinates of the rigid body (Ψ_1).

In general, the orientation of the forces can be chosen in infinitely many ways, but only one choice leads to a symmetrically modelled flexure, which is exactly in the 'middle' of both orientations (Ψ_c) (see Figure 3.1(f)). The orientation of this symmetric coordinate system coincides with the orientation of world coordinates, but rotated $+\frac{1}{2}\varphi$. And it also coincides with the orientation of body coordinates, but rotated $-\frac{1}{2}\varphi$. Only in this case the flexure is modelled symmetrically. Swapping the terminals of the spring now does result in the same spring behaviour. Hence, the flexure is modelled symmetrically. However, the stiffness properties have become dependant on the angular deflection φ.

3.2 Construction of a flexure model, based on 1 DOF springs

The body-editor is a graphical editor in which a rigid body model (or multibody model) can be created. In such a model, rigid bodies (with a certain mass, inertia and centre of mass (COM)) can be connected to each other through joints, in a user friendly way. Compared to modelling rigid bodies with 6-dimensional bond graphs, modelling with the body-editor is much easier, faster and less sensitive to mistakes. Currently, only 1-dimensional joints were implemented in the body-editor. In a later stage, the program will be expanded with multidimensional joints, since the body-editor is still in development.

Springs are not yet implemented in the body-editor. The way to model a 1D spring is to use a joint in the body-editor and connect a spring to the power port of the joint in 20-sim. In principle, a 1 DOF joint is an ideal joint, representing infinite stiffness in all other directions. Each 1 DOF joint may have its own power-port (consisting of an effort and flow) in 20-sim, to which for example dampers or springs can be connected. For mechanical translation, the effort is force and the flow is velocity. For mechanical rotation, the effort is torque and the flow is angular velocity. If a stiffness (C-type element) is connected to the power-port of a joint, the joint behaves as an ideal spring. The C-type element integrates the velocity to a deflection ($x = \int vdt$) and, in the case of a linear stiffness, multiplies the deflection with the stiffness ($k_x \cdot x = F_x$), which is equal to the resulting force. More generally, the force is the partial derivative of the energy function of the spring, no matter whether its stiffness is linear or non-linear: $F_x(x) = \frac{\partial E}{\partial x}$.

To model the compliant flexure behaviour, the flexure is seen as two massless rods, with a 3 DOF spring in between. There are two methods to define a multidimensional spring in the body-editor. Method 1 (which is the normal method) is connecting a 6 DOF C-element to the power interaction ports of two rigid bodies and constrain the out-of-plane DOFs. Rigid bodies may have such a 6 DOF power interaction port, which appears in the resulting equation submodel in 20-sim. To this port, a multidimensional force (and/or torque) source may be connected for example.

Method 2 is constructing the spring from a series connection of 1D joints and let the axes of the joints cross in one point. A 3 DOF flexure, which is constrained in the out-of-plane directions, can be constructed from a series connection of three 1 DOF joints. However, in general a 6 DOF spring cannot be constructed in this way, because it is well-known that a series connection of three 1D rotational joints always gives problems (the order does matter and the construction may end up in a gimbal lock, for example). But since method 1 gave some numerical problems in simulations (drift in the spring position as well as numerical instabilities), method 2 is still used. The joints that construct an in-plane flexure would logically be the three in-plane joints: two translational (along x and y) and one rotational (about z). However, other constructions are possible, for example two rotational joints and a translational joint in between (see Appendix B.3).

A series connection of translational 1D joints does not give problems. The order of joints does not matter, as is shown in Figures 3.2(a) and 3.2(b); the distance between the rigid body and the fixed world is the same for both multidimensional joints. A problem arises when rotational joints are involved. For example, when two translational joints and one rotational joint are connected in series. In this case, it does matter in which order the joints are connected, because the distance between the rigid body and the fixed

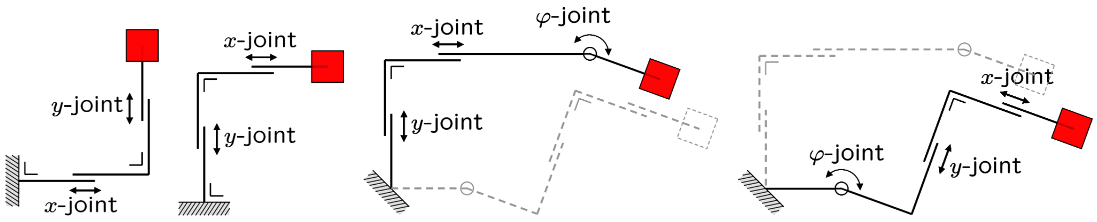

(a) x, y (b) y, x (c) y, x, φ (d) φ, y, x

Figure 3.2: Series connection of joints

world is different. This is shown in Figures 3.2(c) and 3.2(d). Two different orders of joints are shown here (but more different orders can be thought of).

Mathematically the problem comes out as follows. Matrix multiplications are in general not commutative, but in the special case of homogeneous matrices, which only consist of translations, matrix multiplications are commutative:

$$H(x) = \begin{bmatrix} 1 & 0 & x \\ 0 & 1 & 0 \\ 0 & 0 & 1 \end{bmatrix} \qquad H(y) = \begin{bmatrix} 1 & 0 & 0 \\ 0 & 1 & y \\ 0 & 0 & 1 \end{bmatrix} \tag{3.4}$$

$$H(x)H(y) = H(y)H(x) = \begin{bmatrix} 1 & 0 & x \\ 0 & 1 & y \\ 0 & 0 & 1 \end{bmatrix} \tag{3.5}$$

However, matrix multiplications of homogeneous matrices, consisting of rotations and translations are in general not commutative:

$$H(y)H(x)H(\varphi) \neq H(\varphi)H(y)H(x) \tag{3.6}$$

With $H(\varphi)$ a homogeneous matrix, only consisting of a rotation:

$$H(\varphi) = \begin{bmatrix} \cos(\varphi) & \sin(\varphi) & 0 \\ -\sin(\varphi) & \cos(\varphi) & 0 \\ 0 & 0 & 1 \end{bmatrix} \tag{3.7}$$

Figure 3.3(a) shows a multibody model from a flexure that is constructed by a series connection of joints in the order $(x \rightarrow y \rightarrow \varphi)$. Figure 3.3(b) shows a multibody model from a flexure that is constructed by a series connection of joints in the order $(\varphi \rightarrow x \rightarrow y)$. The joints are interconnected with dummy bodies, having zero mass and inertia. The flexure is clamped to the fixed world on the left side, and on the right side a rigid body is connected to the flexure.

When the joints are connected in the order $(x \rightarrow y \rightarrow \varphi)$, the stiffness matrix seems to be defined in world orientation; the forces F_x, F_y and torque M (which are related to the deflection x, y and rotation φ by this stiffness matrix) seem to have the same orientation as world coordinates. Hence, this flexure is equivalent to the flexure in Figure 3.1(d) and is called the 'world-flexure'. When the joints are connected in the order $(\varphi \rightarrow x \rightarrow y)$, the stiffness matrix seems to be defined in body orientation; the forces F_x, F_y and torque M (which are related to the deflection x, y and rotation φ by this stiffness matrix) seem to have the same orientation as body coordinates. Hence, this flexure is equivalent to the flexure in Figure 3.1(e) and is called the 'body-flexure'. The three joints cannot be connected in such a way that the resulting flexure is symmetrically modelled, like the flexure in Figure 3.1(f).

Figure 3.4(a) shows the flexure again, with three different choices of stiffness matrix coordinates. The Ψ_a coordinates are asymmetric and related to the coordinates from Figure 3.3(a) and 3.1(d). The Ψ_b coordinates are asymmetric and related to the coordinates from Figure 3.3(b) and 3.1(e). The Ψ_c coordinates are the only symmetric coordinates and related to the coordinates from Figure 3.1(f).

Infinitely many choices can be made to measure the distance x and y between the spring terminals (see Figure 3.4(b)), as long as $x^2 + y^2 = r^2$ holds. Viewing the flexure from left to right, a series of four coordinate changes is performed: first a rotation $H(\varphi_1)$, then a translation $H(x)$, then a translation $H(y)$ and then a rotation $H(\varphi_2)$: $H = H(\varphi_1)H(x)H(y)H(\varphi_2)$. The first rotation φ_1 can be chosen in the range $[0 : \varphi]$. The second rotation φ_2 is also in the range $[0 : \varphi]$, but should be equal to $\varphi - \varphi_1$, to make the total rotation φ.

The only symmetric coordinates from this range are the Ψ_c coordinates (see Figure 3.4(c)). Viewing the flexure from left to right, the coordinate changes are $H_c = H(\frac{1}{2}\varphi_c)H(x_c)H(y_c)H(\frac{1}{2}\varphi_c)$. Looking from right to left, the coordinate changes are $H(\frac{1}{2}\varphi_c)H(y_c)H(x_c)H(\frac{1}{2}\varphi_c)$. This is the same, but only x and y are switched. However, this does not matter, as mentioned before (see Figures 3.2(a) and 3.2(b)).

A solution is describing the stiffness matrix in symmetric coordinates, but still using an asymmetric joint-structure to construct the flexure. This solution is given in the next paragraph.

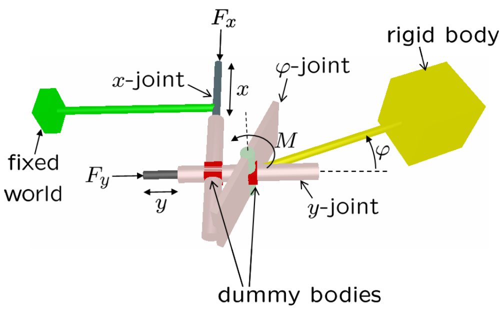

(a) Series connection in the order $(x \rightarrow y \rightarrow \varphi)$

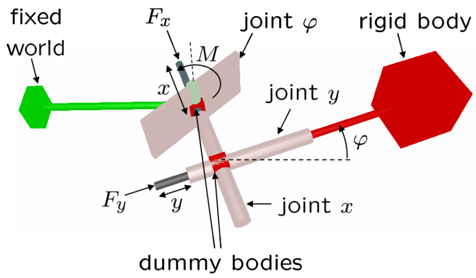

(b) Series connection in the order $(\varphi \rightarrow x \rightarrow y)$

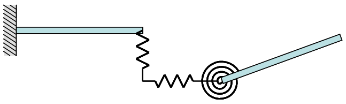

(c) Symbolic representation

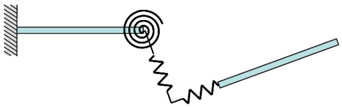

(d) Symbolic representation

Figure 3.3: Flexure model, constructed from 1 DOF springs

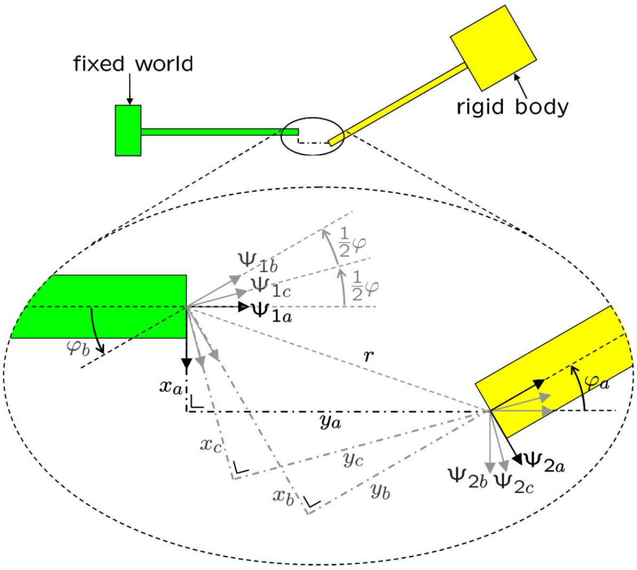

(a) Three different choices of force/torque coordinates

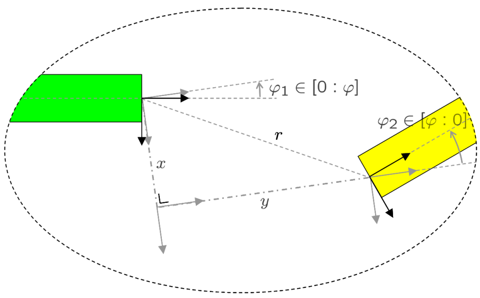

(b) Infinitely many choices of force/torque coordinates

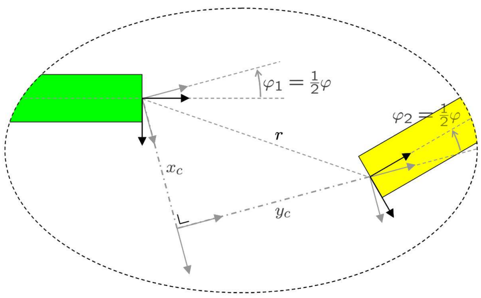

(c) Symmetric force/torque coordinates

Figure 3.4: Different choices of force/torque coordinates

3.3 Symmetric model of a flexure

The energy function of the flexure is expressed in symmetric Ψ_c coordinates. However, symmetric coordinates are not available, in contrast to asymmetric Ψ_a coordinates (or the asymmetric Ψ_b coordinates, depending on the order of the 1D joints, as explained in the previous paragraph). A solution is to rewrite the energy function (Equation 3.3) and express it in Ψ_a coordinates:

$$E = \tfrac{1}{2}\frac{EI}{l}\,\varphi_c^2 + 6\frac{EI}{l}\,x_c^2 + \tfrac{1}{2}\frac{EA}{l}\,y_c^2 \tag{3.8}$$

The relation between (x_c, y_c) and (x_a, y_a) is a rotation of coordinates as can be seen in Figure 3.5:

$$\begin{cases} \varphi_c = \varphi_a \\ \begin{bmatrix} x_c \\ y_c \end{bmatrix} = R_{\frac{1}{2}\varphi} \begin{bmatrix} x_a \\ y_a \end{bmatrix} \end{cases} \quad \Rightarrow \quad \begin{cases} \varphi_c = \varphi_a \\ x_c = x_a\cos(\frac{1}{2}\varphi_a) + y_a\sin(\frac{1}{2}\varphi_a) \\ y_c = -x_a\sin(\frac{1}{2}\varphi_a) + y_a\cos(\frac{1}{2}\varphi_a) \end{cases} \tag{3.9}$$

And substituted in the energy function:

$$E = \tfrac{1}{2}\frac{EI}{l}\,\varphi_a^2 + 6\frac{EI}{l}\,\left(x_a\cos(\tfrac{1}{2}\varphi_a) + y_a\sin(\tfrac{1}{2}\varphi_a)\right)^2 + \tfrac{1}{2}\frac{EA}{l}\,\left(-x_a\sin(\tfrac{1}{2}\varphi_a) + y_a\cos(\tfrac{1}{2}\varphi_a)\right)^2 \tag{3.10}$$

To find the force vector, the energy function has to be differentiated to the coordinates:

$$\begin{aligned} M = \frac{\partial E}{\partial \varphi_a} &= \left(\frac{EI}{l}\right)\varphi + \left(\frac{-3EI\sin(\varphi)}{l^3} + \frac{EA\sin(\varphi)}{4l}\right)x_a^2 \\ &\quad + \left(\frac{6EI\cos(\varphi)}{l^3} - \frac{EA\cos(\varphi)}{2l}\right)x_a y_a + \left(\frac{3EI\sin(\varphi)}{l^3} - \frac{EA\sin(\varphi)}{4l}\right)y_a^2 \end{aligned} \tag{3.11}$$

$$F_x = \frac{\partial E}{\partial x_a} = \left(\frac{12\cos^2(\frac{1}{2}\varphi)EI}{l^3} + \frac{\sin^2(\frac{1}{2}\varphi)EA}{l}\right)x_a + \left(\frac{6\sin(\varphi)EI}{l^3} - \frac{\sin(\varphi)EA}{2l}\right)y_a \tag{3.12}$$

$$F_y = \frac{\partial E}{\partial y_a} = \left(\frac{6\sin(\varphi)EI}{l^3} - \frac{\sin(\varphi)EA}{2l}\right)x_a + \left(\frac{12\sin^2(\frac{1}{2}\varphi)EI}{l^3} + \frac{\cos^2(\frac{1}{2}\varphi)EA}{l}\right)y_a \tag{3.13}$$

These energy-conservative spring equations are put in the C-type element. Since they are non-linear, they cannot be rewritten to matrix from, like in Equation 3.2.

When the flexure rotation is zero and only a deflection occurs, the coordinate systems overlap and the energy functions are the same:

$$E = 6\frac{EI}{l}\,x^2 + \tfrac{1}{2}\frac{EA}{l}\,y^2 \tag{3.14}$$

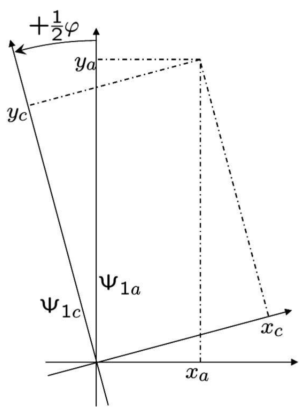

Figure 3.5: $\frac{1}{2}\varphi$ rotation from Ψ_a to Ψ_c

The calculation can be performed for the Ψ_b coordinates as well. But in that case, the stiffness matrix coordinate transformation is a rotation of $-\frac{1}{2}\varphi$ instead of $+\frac{1}{2}\varphi$. The energy function then becomes:

$$E = \tfrac{1}{2}\frac{EI}{l}\,\varphi_b^2 + 6\frac{EI}{l}\,\left(x_b\cos(-\tfrac{1}{2}\varphi_b) + y_b\sin(-\tfrac{1}{2}\varphi_b)\right)^2 + \tfrac{1}{2}\frac{EA}{l}\,\left(-x_b\sin(-\tfrac{1}{2}\varphi_b) + y_b\cos(-\tfrac{1}{2}\varphi_b)\right)^2 \tag{3.15}$$

In the next paragraph a simulation shows that this solution works.

3.4 Simulation of asymmetric and symmetric flexures

To show that the orientation of coordinates of the stiffness matrix matters, a world-flexure (order of springs is $(x \to y \to \varphi)$, see Figure 3.6(a)) is compared with a body-flexure (order of springs is $(\varphi \to x \to y)$, see see Figure 3.6(b)). In the next paragraph both flexures are simulated with a linear spring/stiffness matrix (hence a quadratic energy function). In Paragraph 3.4.2 both flexures are simulated again, but with corrected energy functions (see Equations 3.10 and 3.15). Then, the flexures get similar behaviour and are symmetric.

3.4.1 Asymmetric flexures

The stiffness matrix from Equation 4.19 has been connected to both flexures:

$$K = \begin{bmatrix} 1.09\cdot 10^{-8} & 0 & 0 \\ 0 & 0.0584 & 0 \\ 0 & 0 & 34404 \end{bmatrix} \tag{3.16}$$

They both have a length of 1 mm. The rigid bodies have the mass and inertia of the platform (2.11 µg, see Paragraph 4.3.4). Some damping is modelled to damp out the oscillations. The energy functions of the flexures are quadratic:

$$E = 5.45\cdot 10^{-9}\,\varphi_c^2 + 0.0292\,x_c^2 + 17202\,y_c^2 \tag{3.17}$$

Figure 3.7(a) shows a 3D-plot of this energy function as a function of x_c and y_c, with $\varphi_c = 0.1°$. Figure 3.8 shows a 3D-plot of this energy function as a function of x_c and y_c, with $\varphi_c = 0°$. Visually they are the same, but the second one has an 'offset' of $5.45\cdot 10^{-9}\cdot\left(\frac{0.1\pi}{180}\right)^2 = 1.66\cdot 10^{-14}$ J. The spring equations of this leaf spring are:

$$M' = 1.09\cdot 10^{-8}\,\varphi_c \qquad F_x' = 0.0584\,x_c \qquad F_y' = 34404\,y_c \tag{3.18}$$

The accent distinguishes between the force and torque at the springs (with $'$), and the applied force and torque at the end (without $'$) (see Figures 3.9(e) and 3.9(f)).

A certain force and torque (M, F_x, F_y) (in body orientation) acts at the end of both flexures (see Figure 3.9(a)). The deflection of the body with respect to its origin (its undeformed position) is given in Figures 3.9(b) and 3.9(c). Between 0.015 and 0.04 seconds only a force F_x is applied. Between 0.045 and

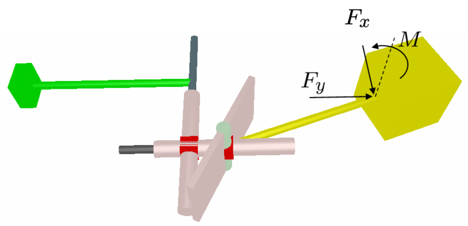

(a) World-flexure: series connection in the order $(x \to y \to \varphi)$ (stiffness matrix is defined in world orientation)

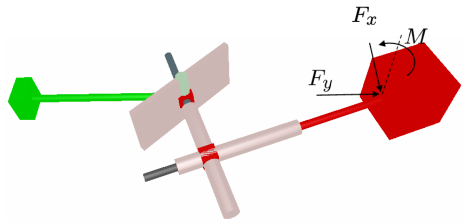

(b) Body-flexure: series connection in the order $(\varphi \to x \to y)$ (stiffness matrix is defined in body orientation)

Figure 3.6: Flexures, constructed from 1 DOF springs

0.065 seconds the same force is applied, together with a torque M such that the rotation φ is just cancelled and a deflection $x = 13.7\,\mu\text{m}$ remains. This can be calculated as follows:

$$\begin{aligned} &\begin{cases} F_x = 0.8\,\mu\text{N} \\ M = 4 \cdot 10^{-10}\,\text{Nm} \end{cases} \Rightarrow \begin{cases} F'_x = 0.8\,\mu\text{N} \\ M' = M - F_x \frac{1}{2} l = 0 \end{cases} \\ \Rightarrow &\begin{cases} x' = \frac{F'_x}{k_x} = \frac{0.8\,\mu\text{N}}{0.0584} = 13.7\,\mu\text{m} \\ \varphi' = 0 \end{cases} \Rightarrow \begin{cases} x = x' + \frac{1}{2} l \sin(\varphi') = 13.7\,\mu\text{m} \\ \varphi = \varphi' = 0 \end{cases} \end{aligned} \tag{3.19}$$

The applied force at the end of the flexure creates a torque in the middle, which exactly compensates for the applied torque at the end. Between 0.07 and 0.095 seconds only a moment is applied.

Schematic representations with deformed springs of the flexures at different time instances are given in Figures 3.9(e) and 3.9(f). To give insight in which 1D spring is deformed, undeformed 1D springs (springs which do not feel any force at that moment) are not shown in these figures.

The deflections of both flexures indeed differ. The difference between the deflections is shown in Figure 3.9(d), which is 0.036 μm and 0.50 μm in x and y-direction. Between 0.01 and 0.04 seconds, only a force in x-direction is applied, which results in a torque and force at the centre of the flexure. For the world-flexure holds that F_x is acting totally on the x-spring, but for the body-flexure holds that F_x is divided between the x-spring and y-spring. Therefore, the x-deflection of the world-flexure is bigger than that of the body-flexure.

As long as the rotation is zero, the coordinate systems in which the stiffness matrices are described, overlap. This is obvious in Figure 3.4(a). When $\varphi = 0$ then $x_a = x_b = x_c$ and $y_a = y_b = y_c$. The simulation also shows this between 0.045 and 0.065 seconds; the flexure deflections are the same.

The difference is only 0.036 μm and 0.50 μm in x and y-direction, but increases rapidly for bigger rotations. For rotations about five times bigger ($\pm 10°$), the difference is already 4.8 μm and 13 μm.

3.4.2 Symmetric flexures

The simulation is performed again, but the stiffness matrices are replaced by the non-linear stiffness equations (Equations 3.11, 3.12 and 3.13). The energy functions of the springs are calculated for this numerical example. The energy function of the world-flexure is (see Equation 3.10):

$$\begin{aligned} E_{world} = 5.45 \cdot 10^{-9} \varphi_a^2 + 2.92 \cdot 10^{-2} (x_a \cos(\tfrac{1}{2}\varphi_a) + y_a \sin(\tfrac{1}{2}\varphi_a))^2 \\ + 1.72 \cdot 10^5 (-x_a \sin(\tfrac{1}{2}\varphi_a) + y_a \cos(\tfrac{1}{2}\varphi_a))^2 \end{aligned} \tag{3.20}$$

Figure 3.7(b) shows a 3D-plot of this energy function as a function of x_a and y_a for $\varphi_a = 0.1°$ (and in Figure 3.8 with $\varphi_a = 0°$). The energy function is quadratic for x_a and y_a when $\varphi = 0$, but deviates more and more from the quadratic energy function when φ increases. The energy function of the body-flexure is (see Equation 3.15):

$$\begin{aligned} E_{body} = 5.45 \cdot 10^{-9} \varphi_b^2 + 2.92 \cdot 10^{-2} (x_b \cos(\tfrac{1}{2}\varphi_b) - y_b \sin(\tfrac{1}{2}\varphi_b))^2 \\ + 1.72 \cdot 10^5 (x_b \sin(\tfrac{1}{2}\varphi_b) + y_b \cos(\tfrac{1}{2}\varphi_b))^2 \end{aligned} \tag{3.21}$$

Figure 3.7(c) shows a 3D-plot of this energy function as a function of x_b and y_b for $\varphi_b = 0.1°$ (and in Figure 3.8 with $\varphi_b = 0°$).

Figures 3.10(b) and 3.10(c) show that statically the deflections are the same. The small differences between the deflections that are shown in Figure 3.10(d) only occur during changes in force and torque. Because of the small rotations possible in the manipulator, only a small error is made when asymmetric flexures are implemented instead of the symmetric ones.

Figures 3.10(e) and 3.10(f) show the power-flow through the flexures and the buffered energy. The energy starts at zero and goes back to zero, which implies no energy is consumed or generated. The energy is totally generated by the sources, consumed by the dampers and buffered by the flexure/spring.

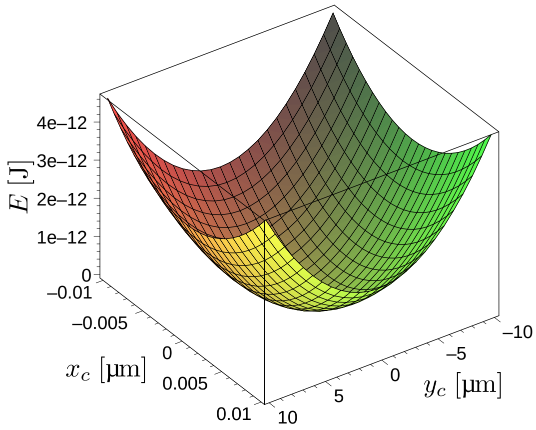

(a) Quadratic energy function

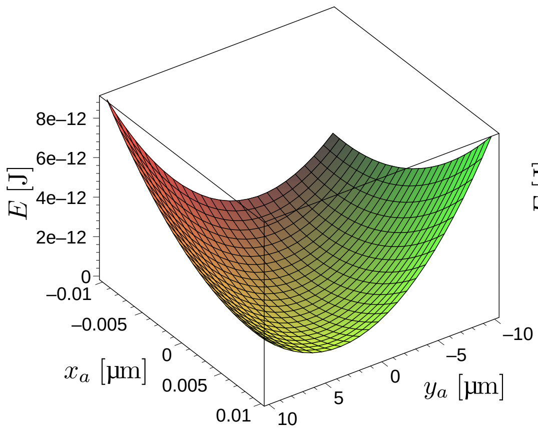

(b) Transformed energy function

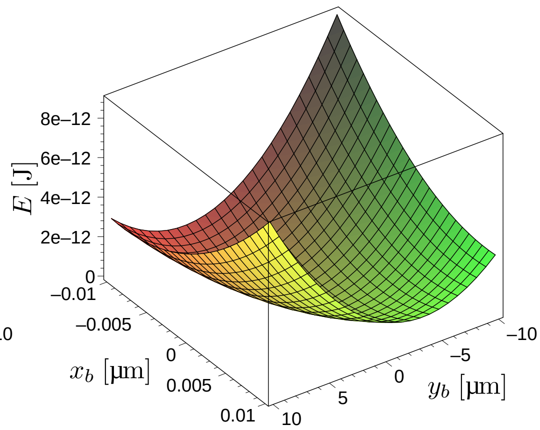

(c) Transformed energy function

Figure 3.7: Energy function as a function of x and y, with $\varphi = 0.1°$

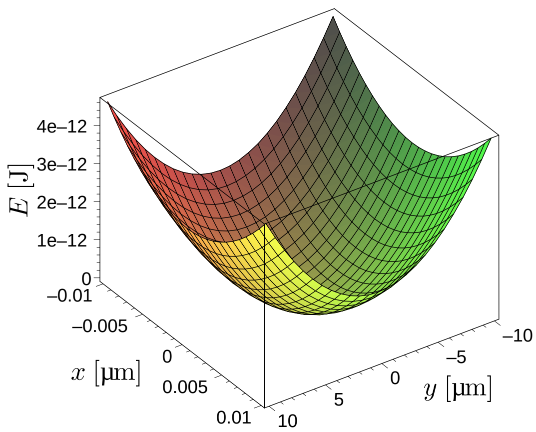

Figure 3.8: Energy functions as a function of x and y, with $\varphi = 0°$ (they overlap)

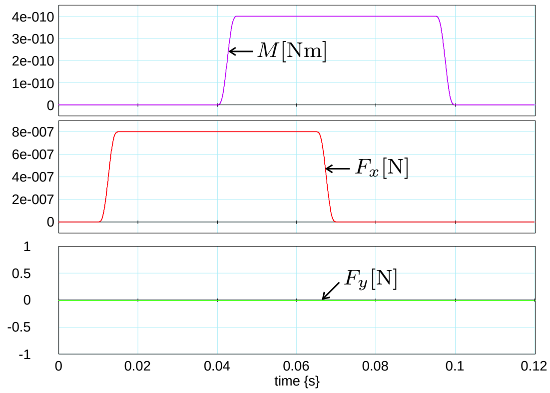

(a) Force and torque, acting at the end of the flexure

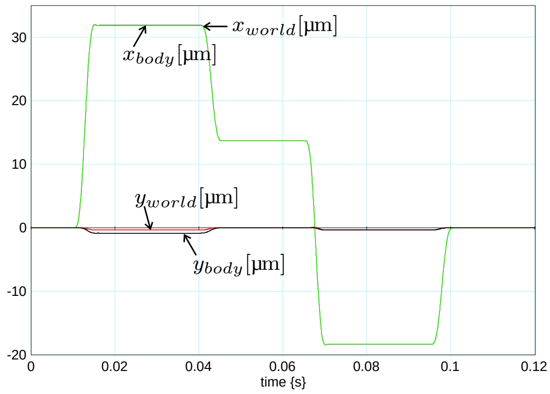

(b) x and y deflection of the flexure

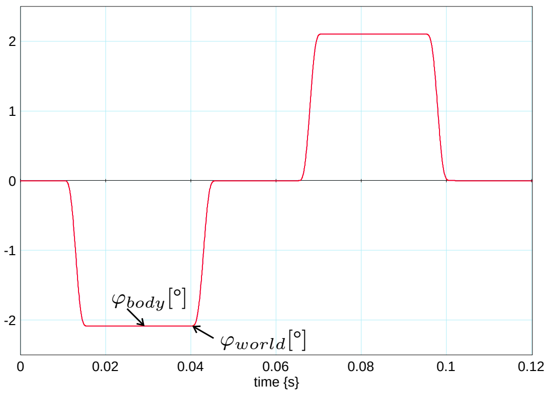

(c) Rotation of the flexure

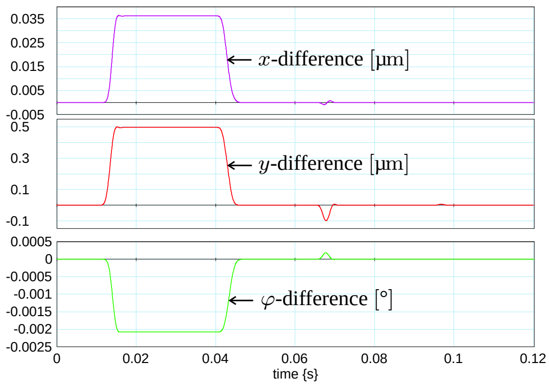

(d) Difference in deflection between both flexures

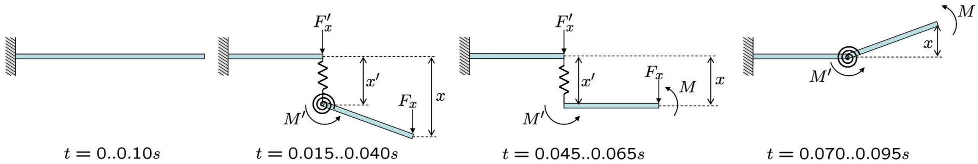

(e) World-flexure ($x \rightarrow y \rightarrow \varphi$), at different time instances

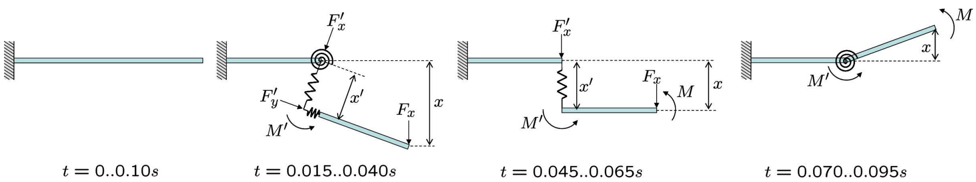

(f) Body-flexure ($\varphi \rightarrow x \rightarrow y$), at different time instances

Figure 3.9: Simulation of two asymmetric flexures

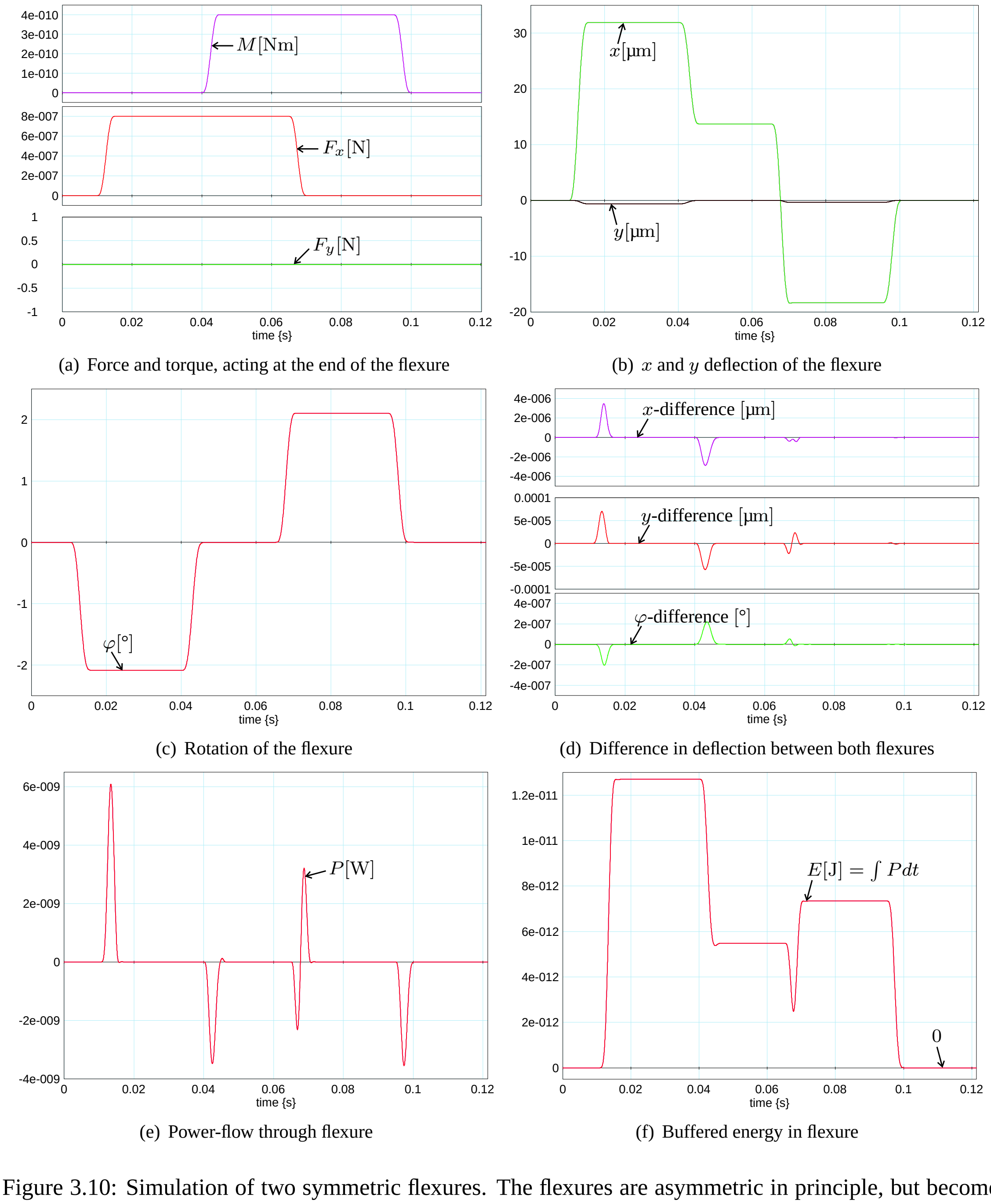

(a) Force and torque, acting at the end of the flexure

(b) x and y deflection of the flexure

(c) Rotation of the flexure

(d) Difference in deflection between both flexures

(e) Power-flow through flexure

(f) Buffered energy in flexure

Figure 3.10: Simulation of two symmetric flexures. The flexures are asymmetric in principle, but become symmetric due to the transformed stiffness matrices

3.5 Reinforced flexures

Instead of flexures with a fixed thickness, reinforced flexures transfer forces to the platform. These flexures have a reinforced mid-section which not only leads to an increase in all stiffnesses (see Soemers [7]):

$$K = \begin{bmatrix} k_\varphi & 0 & 0 \\ 0 & k_x & 0 \\ 0 & 0 & k_y \end{bmatrix} = \begin{bmatrix} \frac{EI}{l}\left(\frac{1}{1-p}\right) & 0 & 0 \\ 0 & 12\frac{EI}{l^3}\left(\frac{1}{1-p^3}\right) & 0 \\ 0 & 0 & \frac{EA}{l}\left(\frac{1}{1-p}\right) \end{bmatrix} \tag{3.22}$$

But also leads to a slower decrease in k_y as a function of the x-displacement, according to v.Eijk [4]:

$$\frac{k_y}{k_{y,0}} = \frac{1}{1 + \frac{12x^2}{(1-p)Bd^2}} \tag{3.23}$$

With:

$$B = 700\frac{(1+q)(1+3q+3q^2)^3}{1+10q+45q^2+105q^3+105q^4} \qquad \text{and} \qquad q = \frac{p}{1-p} \tag{3.24}$$

Which is an advantage of reinforced flexures, as well as the increase in longitudinal stiffness. A disadvantage is that the lateral and rotational stiffnesses both increase.

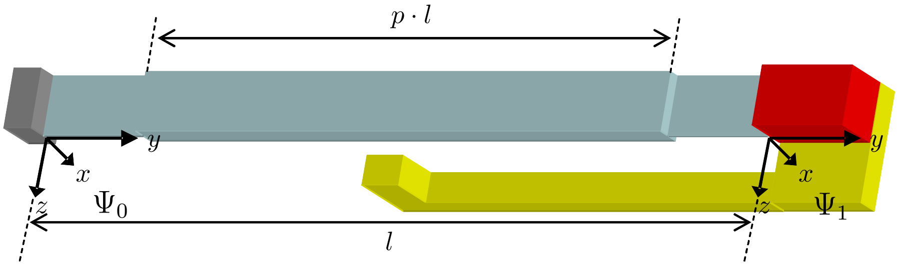

(a) Undeformed reinforced flexure (rotated about y with respect to flexures below)

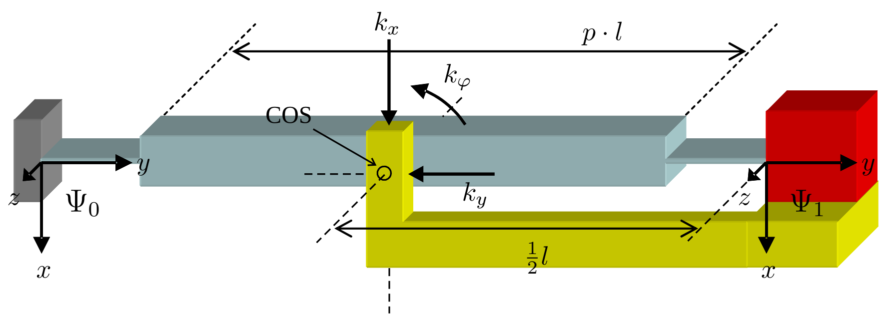

(b) Undeformed reinforced flexure

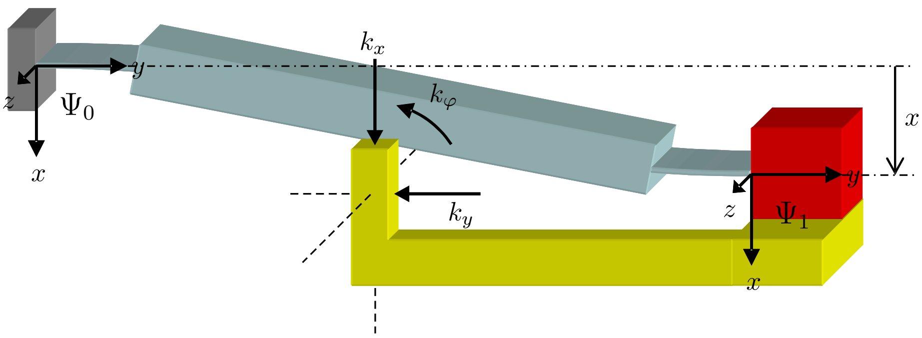

(c) Deformed reinforced flexure due to a positive force F_x (M and F_y are zero)

Figure 3.11: Reinforced flexure

Chapter 4

Power-port modelling & simulation

In this chapter the 20-sim model of the manipulator is addressed. Paragraph 4.1 explains the multibody model that was created in the body-editor. In Paragraph 4.2 the 20-sim model is treated. Parameters like masses, inertias and stiffnesses are calculated in Paragraph 4.3. In Paragraph 4.4 the stiffness and resonance frequencies of the manipulator are simulated with 20-sim.

4.1 Multibody model

The multibody model of the in-plane manipulator is given in Figure 4.1. The dimensions of the squares in the grid are 0.5×0.5 mm. Three arms are connected to a triangular platform in parallel. The little cross in the origin of the world coordinate system is the reference body. It is fixed to the fixed world, so does not move. The guiding direction of the folded flexures and the direction the comb-drive moves are represented by translational joints. These are connected to the reference and the shuttles. The construction only allows in-plane movement of the platform (i.e. translation along x and y and rotation about z).

Figure 4.2 shows a schematic representation of the multibody model. It visualizes more clearly how the flexures are constructed in the body-editor. The comb-drives excite a force F_{comb} on the shuttle. The shuttle is connected to the fixed world through a spring on one side, which represents the lateral stiffness of each set of four folded flexures. On the other side, it is connected to a massless rod. The platform is also connected to a massless rod. Both rods are connected to each other through two translational springs, one rotational spring and two dummy bodies (having zero mass and inertia), which represent the in-plane compliant behaviour of the flexure. Unlike in the scheme, the axes of translation and rotation for the flexure coincide in the multibody model.

The scheme already shows springs instead of joints, but the multibody model does not contain springs, since they are not implemented in the body-editor yet (as mentioned in Paragraph 3.2). The multibody model only contains the rigid bodies (with their positions, masses and inertias), and the kinematic construction of joints and rigid bodies. The compliant behaviour of the flexures is added in 20-sim.

4.2 20-sim model

Figure 4.4 shows the total 20-sim model of the manipulator. The comb-drive & folded flexure part and the flexure part of the model will be explained in the next paragraphs. Finally, the total model is explained.

4.2.1 Comb-drive & folded flexure part

Figure 4.3(a) shows the comb-drive and folded flexure part of the 20-sim model of the manipulator. A force source, spring and damper is connected to the power-port of each of the three translational (comb-drive) joints.

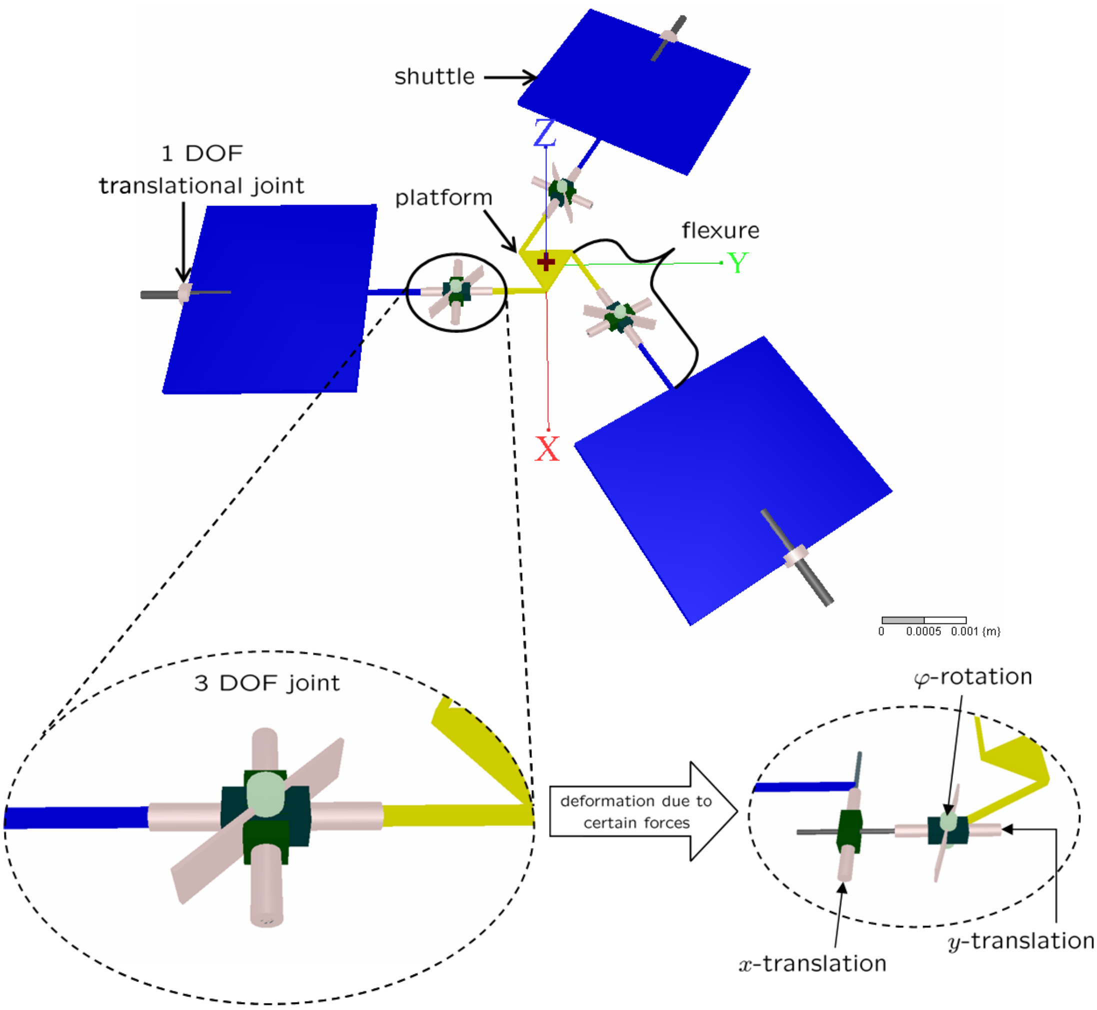

Figure 4.1: Multibody model

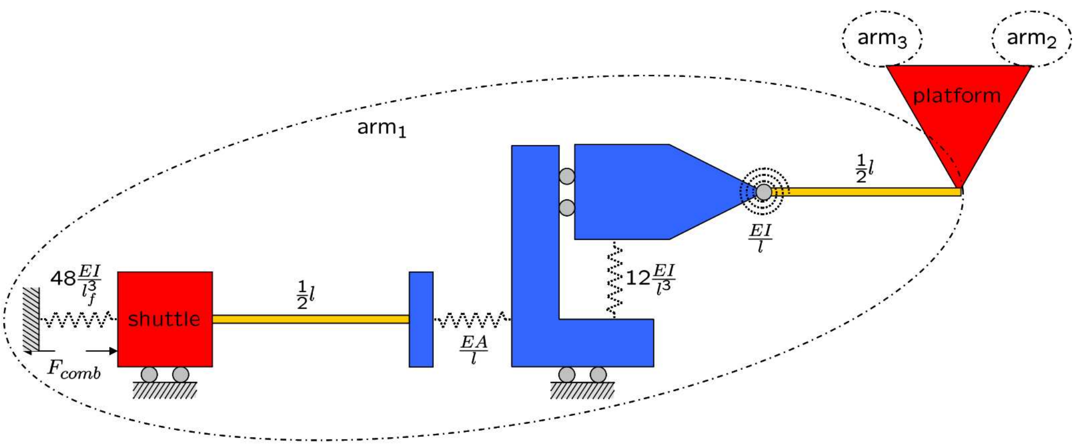

Figure 4.2: Schematic representation of multibody model

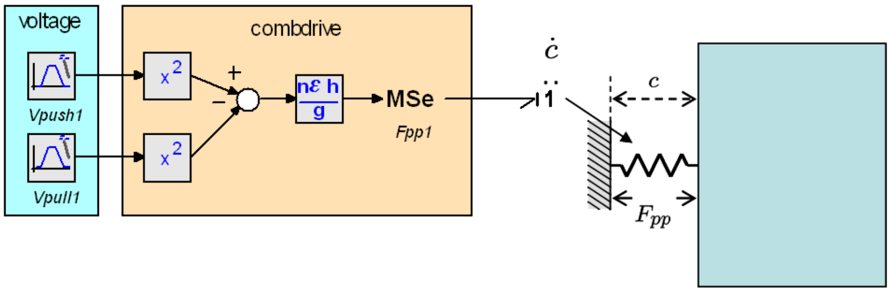

(a) 20-sim model of comb-drive

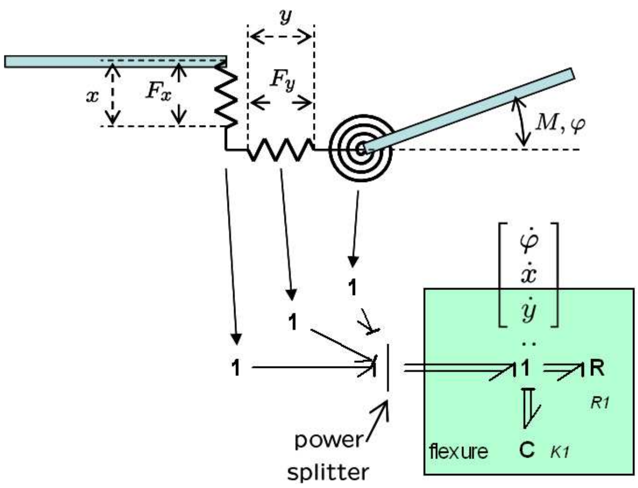

(b) 20-sim model of flexure

Figure 4.3: Parts of 20-sim model

The force source (MSe) represents the force generated by a set of two comb-drives. They are excited with a smooth voltage profile. Voltage steps should never be put on a comb-drive in reality, because of the low damping in the manipulator (only some material damping and air friction). A voltage step will result in big oscillations of the platform, which is undesired. Hence in the model, also a smooth voltage is used.

The push and pull voltage are both squared and subtracted from each other. The results is multiplied with $\frac{n\epsilon h}{g}$ to end up with the force generated by both comb-drives. This is exactly what the force-voltage relation showed (see also Equation 2.2):

$$F_{pp} = \frac{n\epsilon h}{g}\left(V_{push}^2 - V_{pull}^2\right) \tag{4.1}$$

Comb-drive pull-in occurs very often with these kind of devices, which will break it. Therefore the side-instability voltage was calculated. Legtenberg [2] gives an expression for the voltage at which side-instability occurs:

$$V_{side} = \sqrt{\frac{g^2 k_g}{2\epsilon_0 hn}\left(\sqrt{2\frac{k_l}{k_g} + \frac{c_0^2}{g^2}} - \frac{c_0}{g}\right)} = 415\,\mathrm{V} \tag{4.2}$$

This is promising, because it is a very high voltage. One remark is that the longitudinal stiffness of the folded flexures (k_l) decreases as a function of the comb-drive deflection. The following relation is given by v.Eijk [4]:

$$\frac{k_l}{k_{l,0}} = \frac{1}{1 + \dfrac{12x^2}{700d^2}} \tag{4.3}$$

The maximum deflection of the manipulator stays within $\pm 10\,\mu\mathrm{m}$, which results in a decrease in k_l with a factor 0.7. But then, the side-instability voltage still is $379\,\mathrm{V}$, which is still very high. Hence, no problems are expected considering pull-in.

Ideally, the movable part (rotor) and the stationary part (stator) of a comb-drive are perfectly aligned so the gap between rotor and stator is the same on both sides. This ideal situation is assumed in above calculations. However, the side-instability voltage decreases rapidly due to misalignment between rotor and stator (see [9]).

4.2.2 Flexures / leaf springs part

Figure 4.3(b) shows the flexure part of the 20-sim model of the manipulator. For each flexure, the three power-ports of the joints are put together in a 3D-bond, using a power splitter. A stiffness (C-element) and damper (R-element) are connected to the 3D-bonds, which represents the flexure's compliant behaviour. Almost no damping exists in the real manipulator (only some material damping and air friction), but a higher damping makes simulations faster, which is handy to simulate static behaviour. Dynamic behaviour is not as important as static behaviour, because the manipulator does not need to be very fast.

The compliant behaviour of the flexure is only linear in a small range around equilibrium. In this linear range, a constant stiffness-matrix K may represent the spring. A linear spring integrates the velocities $(\dot{\varphi}, \dot{x}, \dot{y})$ to deflections (φ, x, y) and multiplies it with K, which is equal to the force and torque.

However, the flexure is non-linear and described by a non-linear energy function (see Equation 3.10), so a single stiffness matrix is not sufficient. Instead of a stiffness matrix, the partial derivatives of the energy function to φ, x and y (Equations 3.11, 3.12 and 3.13) are put in the C-element. (These equations are related to each other by the energy function of the spring and cannot be random functions). This ensures that the C-element only buffers energy like an ideal spring, and does not consume or generate energy.

4.2.3 Total model

Figure 4.4 shows the total 20-sim model of the manipulator. The multibody model from the body-editor is imported in 20-sim as an equation submodel. In subblock 'Hp', the homogeneous matrix (consisting the position and orientation) of the platform with respect to the fixed world is monitored. Each joint has its own power port, consisting of an effort and flow (power = effort × flow). The power-port of a translational joint consists of an effort F, which is the relative force between the two parts of a joint; and a flow v, which is the relative velocity between the two parts of the joint. The time-integral of this velocity is the relative deflection of the joint.

4.3 Parameters

4.3.1 General dimensions

The most important dimensions with their symbols, which are used throughout this report, are given in Table 4.1. The thickness of the reinforced flexures, the folded flexures and the comb-drive teeth is 2 µm by design, but varies in reality (because of the mask resolution, varying etch times, and so on).

4.3.2 Properties of silicon

The density of silicon (ρ_{si}) is $2.33 \cdot 10^3\ \mathrm{kg}/\mathrm{m}^3$. The so-called twin-etching method requires that the shuttles and the platform contain square holes of $9 \times 9\,\mu\mathrm{m}$ in a raster of $12 \times 12\,\mu\mathrm{m}$. This leads to a decrease in mass with a so-called 'hole'-factor $f = 0.4375$.

Since silicon is an anisotropic material, its Young's modulus is direction dependent. Kaajakari [3] uses tensor formalism to calculate Young's modulus for silicon. With the free downloadable matlab script, the Young's modulus can be calculated for different angles in the $[1\,0\,0]$-plane (see Figure 4.5), which corresponds to the silicon wafer plane. The folded flexures and leaf spring of Arm_1 lay in the $[1\,0\,0]$-direction (or $[0\,1\,0]$, which is equivalent), in contradiction to the folded flexures and leaf springs of Arm_2 and

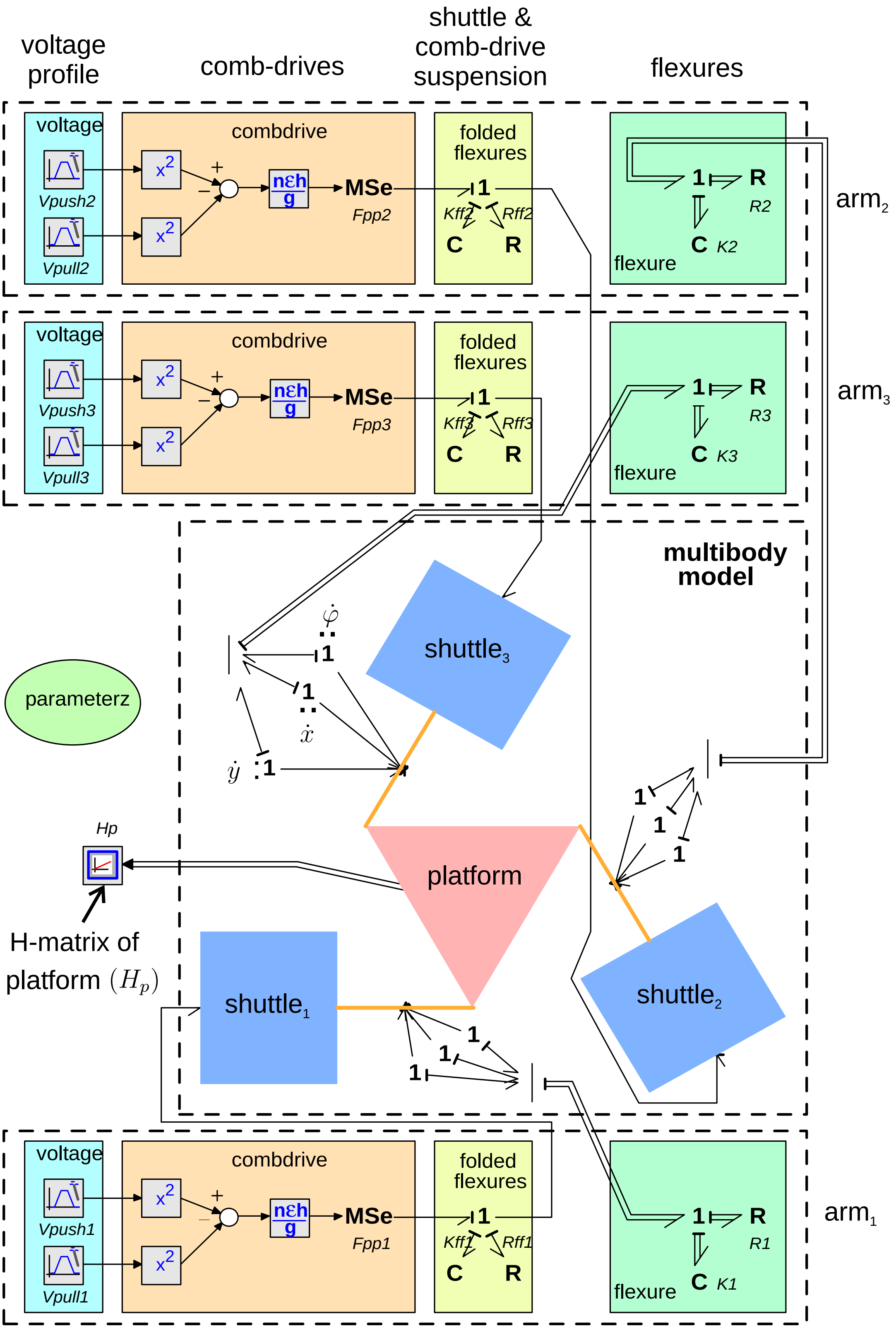

Figure 4.4: 20-sim model of manipulator

structure			dimension	symbol
all structures	height (in direction perpendicular to wafer)		$38\,\mu m$	h
shuttle	length		$1200\,\mu m$	
	width		$940\,\mu m$	
reinforced flexure	total length		$1\,mm$	l_s
	thin section	width	$2\,\mu m$	d
	thick section	width	$14\,\mu m$	
		length	$720\,\mu m$	
comb-drive	tooth	thickness	$2\,\mu m$	d
		length	$50\,\mu m$	
		initial overlap	$20\,\mu m$	c_0
	gap		$4\,\mu m$	g
folded flexure	length		$400\,\mu m$	l_f
	width		$2\,\mu m$	d

Table 4.1: General dimensions

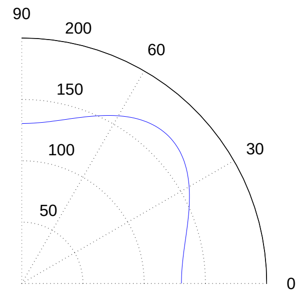

Figure 4.5: Young's modulus (GPa) in the $[1\,0\,0]$-plane

Arm$_3$ which make an angle of 30° or 60° with the $[1\,0\,0]$-direction. This can be called the $[1\sqrt{3}\,0]$-direction (or $[\sqrt{3}\,1\,0]$, which has the same Young's modulus). Young's modulus in the two important directions:

$$E_{[1\,0\,0]} = 130\,\mathrm{GPa} \qquad E_{[1\sqrt{3}\,0]} = 158\,\mathrm{GPa} \tag{4.4}$$

4.3.3 Shuttle

A rigid body is fully described by a mass and inertia matrix, and its 'center of mass' (COM). The mass of the shuttle is:

$$m_s = \rho_{si} \cdot A \cdot h \cdot f = 3.98 \cdot 10^{-8}\,\mathrm{kg} = 40.4\,\mu\mathrm{g} \tag{4.5}$$

With ρ_{si} the density of silicon, A the surface of the shuttle (which has been corrected for the space the folded flexures take), h the height of the shuttle and f the hole-factor. The mass of the reinforced flexure is:

$$m_f = \rho_{si} \cdot h \left(\underbrace{\overbrace{14\,\mu\mathrm{m}}^{\text{width}} \cdot \overbrace{720\,\mu\mathrm{m}}^{\text{length}} \cdot \overbrace{\frac{14^2 - 9^2}{14^2}}^{\text{hole factor}}}_{\text{reinforced part}} + \underbrace{\overbrace{2\,\mu\mathrm{m}}^{\text{width}} \cdot \overbrace{280\,\mu\mathrm{m}}^{\text{length}}}_{\text{thin part}} \right) = 5.7 \cdot 10^{-10}\,\mathrm{kg} = 0.57\,\mu\mathrm{g} \tag{4.6}$$

To account for this mass in the model, it has been added to the mass of the shuttle.

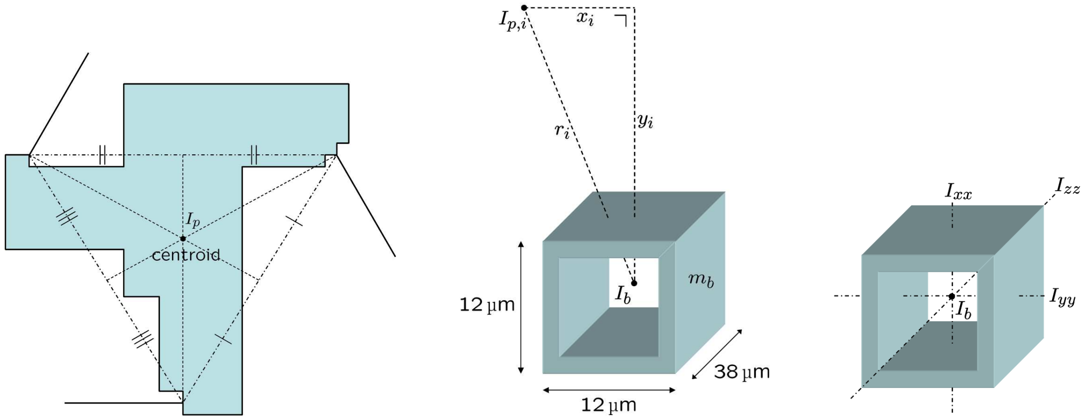

(a) Platform

(b) Inertia of one block around the platform's centroid

(c) Inertia of one block around its COM (in principal axes)

Figure 4.6: Inertia of platform

The shuttle is a rectangular body with mass m and dimensions $a \times b \times h$. The inertia matrix of the shuttle (in its COM and with principal axes perpendicular and parallel to the body) is:

$$I_s = \frac{1}{12} m_s \begin{bmatrix} b^2 + h^2 & 0 & 0 \\ 0 & a^2 + h^2 & 0 \\ 0 & 0 & a^2 + b^2 \end{bmatrix} = \begin{bmatrix} 5.25 & 0 & 0 \\ 0 & 3.22 & 0 \\ 0 & 0 & 8.46 \end{bmatrix} 10^{-15} \tag{4.7}$$

4.3.4 Platform

Figure 4.6(a) shows a schematic figure of the platform. The reinforced flexures are connected to the platform in a isosceles triangle. The inertia matrix of the platform (I_p) around the centroid of the triangle (geometrical center) is calculated in this paragraph. The platform consists of $n = 378$ small blocks of $12 \times 12 \times 38\,\mu\text{m}$. The mass of one block is:

$$m_b = \rho_{si} \cdot 12\,\mu\text{m} \cdot 12\,\mu\text{m} \cdot 38\,\mu\text{m} \cdot f = 5.58 \cdot 10^{-12}\,\text{kg} \tag{4.8}$$

And the mass of the platform is:

$$m_p = n \cdot m_b = 2.11 \cdot 10^{-9}\,\text{kg} = 2.11\,\mu\text{g} \tag{4.9}$$

The inertia matrix of the platform in the centroid is calculated by summing the inertia matrices of the small blocks that build up the platform. The inertia matrix of block i around the centroid of the platform (see Figure 4.6(b)) is calculated by the parallel axes rule: $I_{p,i} = I_b + m_b r_i^2$. The inertia matrix of the platform is the sum of all inertia matrices:

$$I_p = \sum_{i=1:n} I_{p,i} = \sum_{i=1:n} \left(I_b + m_b r_i^2\right) = nI_b + m_b \sum_{i=1:n} r_i^2 \tag{4.10}$$

With:

$$r_i^2 = \begin{bmatrix} y_i^2 + z_i^2 & -x_i y_i & -x_i z_i \\ -x_i y_i & x_i^2 + z_i^2 & -y_i z_i \\ -x_i z_i & -y_i z_i & x_i^2 + y_i^2 \end{bmatrix} = \begin{bmatrix} y_i^2 & -x_i y_i & 0 \\ -x_i y_i & x_i^2 & 0 \\ 0 & 0 & x_i^2 + y_i^2 \end{bmatrix} \tag{4.11}$$

Which has been calculated for each block in a Matlab script. The inertia matrix of one block in its COM is (see Figure 4.6(c)):

$$I_b = \frac{m_b}{12}\begin{bmatrix} 12^2+38^2 & 0 & 0 \\ 0 & 12^2+38^2 & 0 \\ 0 & 0 & 12^2+12^2 \end{bmatrix} \cdot 10^{-12} = \begin{bmatrix} 7.38 & 0 & 0 \\ 0 & 7.38 & 0 \\ 0 & 0 & 1.34 \end{bmatrix} \cdot 10^{-22} \tag{4.12}$$

Finally, the inertia matrix of the platform is:

$$I_p = \begin{bmatrix} 1.72 & -0.19 & 0 \\ -0.19 & 1.27 & 0 \\ 0 & 0 & 2.94 \end{bmatrix} \cdot 10^{-17} \tag{4.13}$$

The whole inertia matrix is calculated, because the body-editor asks for the three principal inertias. But since out-of-plane rotations do not occur, only the inertia for in-plane rotations (I_z) is important.

4.3.5 Reinforced flexures & folded flexures

The stiffnesses of the three reinforced flexures are different, not only because their orientations in silicon result in a different Young's modulus, but also because the average flexure thickness is different. The latter is caused by the resolution of the mask used in the fabrication process, which seemed to be too low. As a result, the borders of flexures under an angle of 30° or 60° are not straight (SEM photos show this in [6]).

Hence, the stiffness matrix has to be calculated separately for the first arm (K_1), and for the second & third arm (K_{23}):

$$K = \begin{bmatrix} \frac{EI}{l_s}\left(\frac{1}{1-p}\right) & 0 & 0 \\ 0 & 12\frac{EI}{l_s^3}\left(\frac{1}{1-p^3}\right) & 0 \\ 0 & 0 & \frac{EA}{l_s}\left(\frac{1}{1-p}\right) \end{bmatrix} \tag{4.14}$$

With A the area of the profile, and I the area moment of inertia, which is $\frac{1}{12}hd^3$ as the flexure has a square profile.

$$d_1 = 1.95\,\mu\mathrm{m} \qquad d_{23} = 1.75\,\mu\mathrm{m} \tag{4.15}$$

$$I_1 = \frac{hd_1^3}{12} = 2.35 \cdot 10^{-23}\,\mathrm{m}^4 \qquad I_{23} = \frac{hd_{23}^3}{12} = 1.70 \cdot 10^{-23}\,\mathrm{m}^4 \tag{4.16}$$

$$A_1 = hd_1 = 7.41 \cdot 10^{-11}\,\mathrm{m}^2 \qquad A_{23} = hd_{23} = 6.65 \cdot 10^{-11}\,\mathrm{m}^2 \tag{4.17}$$

$$E_1 = 130\,\mathrm{GPa} \qquad E_{23} = 158\,\mathrm{GPa} \tag{4.18}$$

The stiffness of the reinforced flexures very much depends on the thickness, because the area moment of inertia depends on the thickness to the third power.

$$K_1 = \begin{bmatrix} 1.09 \cdot 10^{-8} & 0 & 0 \\ 0 & 0.0584 & 0 \\ 0 & 0 & 34404 \end{bmatrix} \qquad K_{23} = \begin{bmatrix} 9.58 \cdot 10^{-9} & 0 & 0 \\ 0 & 0.0513 & 0 \\ 0 & 0 & 37525 \end{bmatrix} \tag{4.19}$$

The guiding stiffness of the comb-drive suspension (which are folded flexures) is $48\frac{EI}{l_f^3}$. They also depend on the orientation in silicon:

$$k_{g_1} = 2.29\,\mathrm{N/m} \qquad k_{g_{23}} = 2.01\,\mathrm{N/m} \tag{4.20}$$

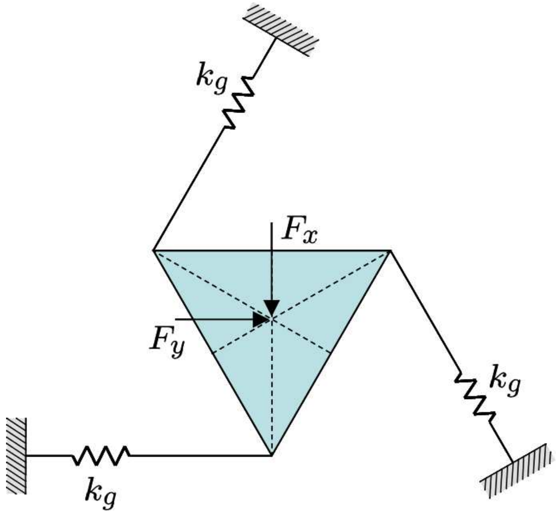

(a) The stiffness the platform 'feels' is dominated by the guiding stiffness of the folded flexures (= shuttle suspension)

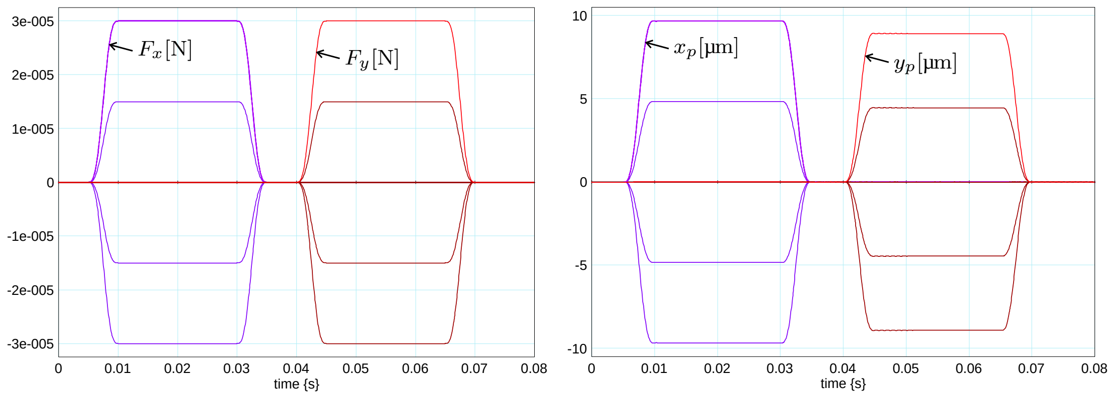

(b) Force acting on the centre of the platform

(c) Deflection of the platform in x and y direction

Figure 4.7: Simulation of the stiffness the platform feels

4.4 Simulation

4.4.1 Stiffness felt by platform

The stiffness the platform 'feels' is simulated by putting a force in the centre of the platform and looking at its deflection (see Figure 4.7), as if the platform is pushed. Figures 4.7(b) and 4.7(c) show a multiple run simulation with $F = \{-30, -15, 0, 15, 30\}$ µN. No voltage is put on the comb-drives in this simulation. The force divided by the deflection is the stiffness the platform feels, which is constant for small deflections:

$$k_{p_x} = \frac{F_x}{x} = \frac{30\,\mu\text{N}}{9.67\,\mu\text{m}} = 3.10\,{}^{\text{N}}/_{\text{m}} \qquad k_{p_y} = \frac{F_y}{y} = \frac{30\,\mu\text{N}}{8.92\,\mu\text{m}} = 3.36\,{}^{\text{N}}/_{\text{m}} \tag{4.21}$$

This is verified by calculations as follows. The most dominant stiffness the platform feels when it moves in translational directions is the guiding stiffness of the folded flexures (k_g) (= shuttle suspension), which is about 40 times bigger than the lateral stiffness of the reinforced flexures. It is easy to calculate that the stiffness the platform feels is $\frac{3}{2}$ times k_g, due to the symmetric structure of the manipulator (see [8]). The average k_g of the three shuttle suspensions is $2.10\,{}^{\text{N}}/_{\text{m}}$. The average stiffness the platform feels is:

$$k_p = \tfrac{3}{2} \cdot k_g = \tfrac{3}{2} \cdot 2.10 = 3.16\,{}^{\text{N}}/_{\text{m}} \tag{4.22}$$

To give an estimation of the manipulator's translational resonance frequencies, the total mass that moves in the translational directions has to be calculated, which is not just the sum of all masses. Similar to the stiffness, the equivalent mass of the three shuttles in translational directions is $\frac{3}{2}$ times m_s. For the total mass, the mass of the platform has to be added:

$$m_{tot} = \tfrac{3}{2} \cdot m_s + m_p = 67.7\,\mu\mathrm{g} \tag{4.23}$$

Hence, the translational resonance frequencies will be about:

$$f_r = \frac{1}{2\pi}\sqrt{\frac{k_p}{m_{tot}}} = 1087\,\mathrm{Hz} \tag{4.24}$$

4.4.2 Resonance frequencies

The resonance frequencies of the platform (in x-direction, y-direction and for φ-rotation) are simulated in order to validate them with measurements in Paragraph 6.2. A sinusoidal force (or torque) with increasing frequency and a fixed amplitude is put on the centre of the platform. The deflections and rotation are plotted in Figure 4.8. The deflection of the platform is maximal at the resonance frequency, which are listed in the table below:

direction	**freq.** (Hz)
φ	1353 ± 10
x	1122 ± 10
y	1163 ± 10

Table 4.2: Simulated resonance frequencies

The resonance frequencies can also be simulated by putting a sinusoidal voltage on the comb-drives. The force frequency is two times the voltage frequency, because of the quadratic force-voltage relation. Hence, the frequency is doubled and an offset is introduced:

$$\left.\begin{array}{l} F \sim V^2 \\ V = V_a \sin(\omega t) \end{array}\right\} \quad F \sim V_a^2 \sin^2(\omega t) = \tfrac{1}{2}V_a^2 - \tfrac{1}{2}V_a^2\cos(2\omega t) \tag{4.25}$$

The resonance frequency depends a little on the damping. Therefore the damping was estimated roughly in another simulation. A sinusoidal voltage with an amplitude of 14 V was put on the comb-drives and the damping-parameter was varied until the simulated and measured deflection at the resonance frequency were about the same. Figure 6.2(a) shows that the deflection at the resonance frequency in x-direction is about 9 µm (peak-peak). In simulations a viscous damping $r = 2.5 \cdot 10^{-5}\,\mathrm{Ns/m}$ for the folded flexures seemed to result in about the same deflection (the damping for the reinforced flexures is left zero for simplicity reasons). The relative damping is about:

$$\zeta = \frac{r}{2\sqrt{mk}} = 2.7\,\% \tag{4.26}$$

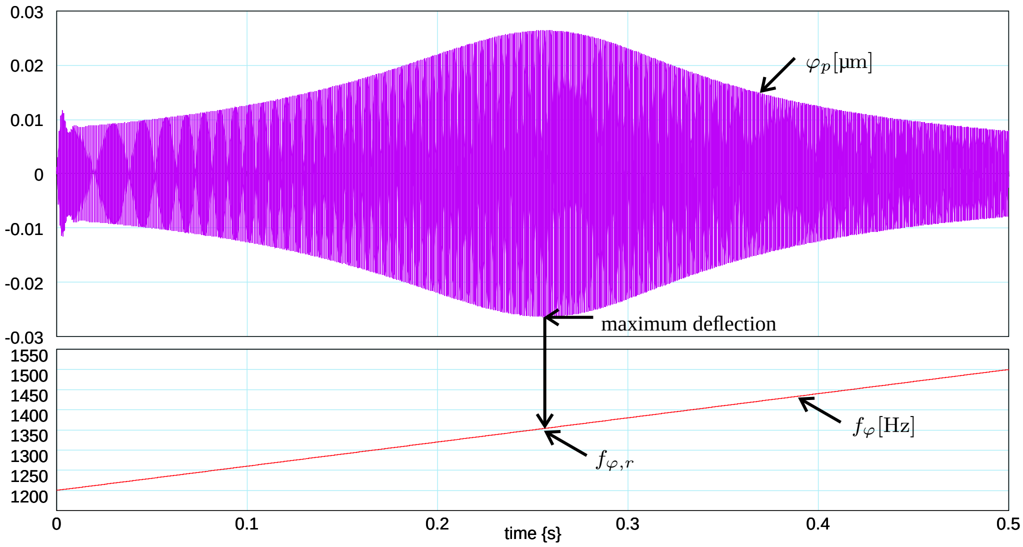

(a) Resonance frequency of platform for φ-rotation

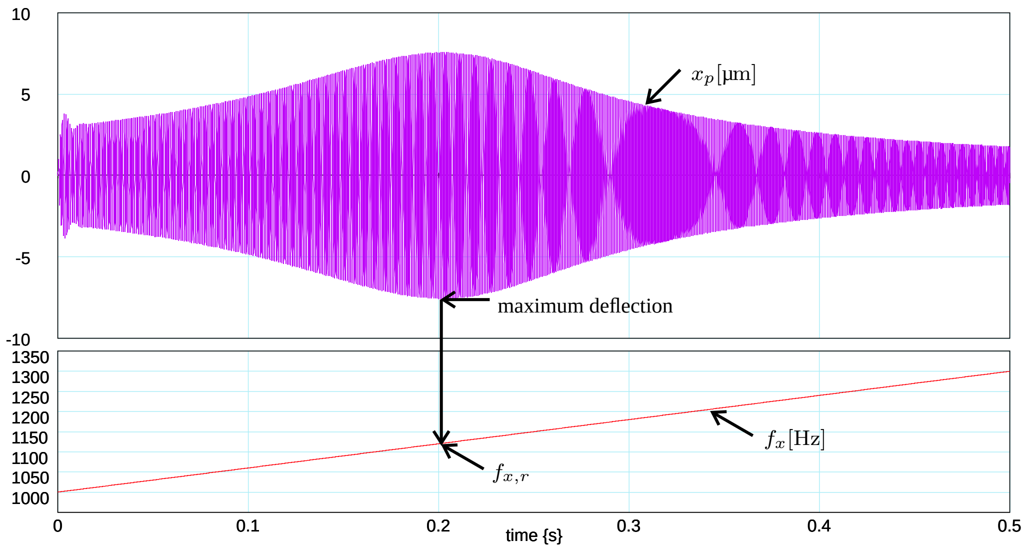

(b) Resonance frequency of platform in x-direction

Figure 4.8: Simulation of the resonance frequency

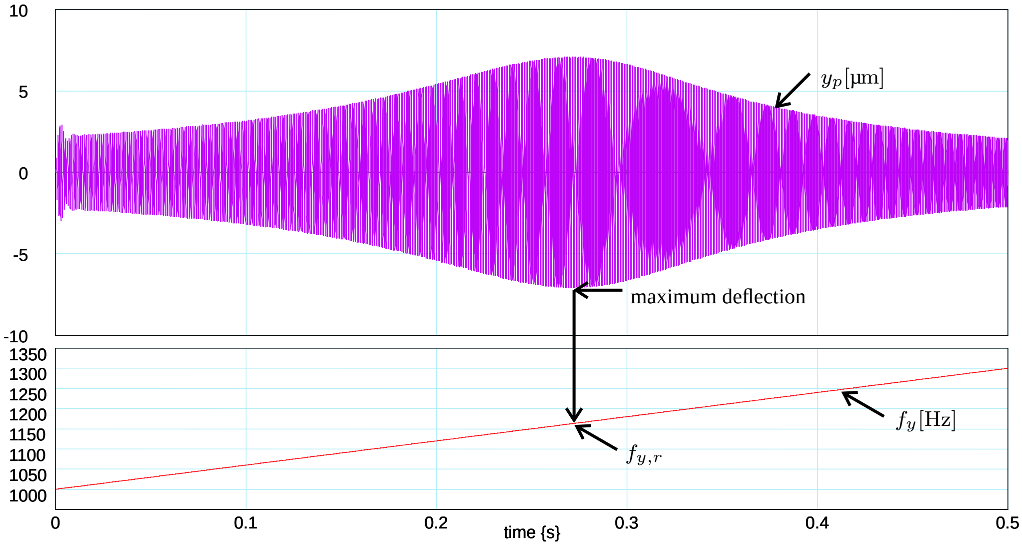

(c) Resonance frequency of platform in y-direction

Figure 4.8: Simulation of the platform's resonance frequencies

Chapter 5

Feed-forward position control

With the voltage controlled model, three voltages are input and the platform will move in a certain direction, depending on the comb-drive strength and the dynamics of the system. However, it is not clear beforehand how much volt to put on which comb-drive to let it move in e.g. only the x-direction. Instead of comb-drive voltages, the desired platform position should be used as input. Hence, what is needed, is a mapping from platform position to comb-drive voltage:

$$\begin{bmatrix} x_{p\_sp} \\ y_{p\_sp} \\ \varphi_{p\_sp} \end{bmatrix} \mapsto \begin{bmatrix} V_{comb_1} \\ V_{comb_2} \\ V_{comb_3} \end{bmatrix} \tag{5.1}$$

An inverse kinematic model (IKM) of the system could give a mapping from platform position to comb-drive deflection:

$$\begin{bmatrix} x_{p\_sp} \\ y_{p\_sp} \\ \varphi_{p\_sp} \end{bmatrix} \mapsto \begin{bmatrix} c_1 \\ c_2 \\ c_3 \end{bmatrix} \tag{5.2}$$

And since the comb-drive deflection is proportional to the force of the comb-drive and proportional to the square of the comb-drive voltage:

$$c_i \sim \begin{bmatrix} F_{comb_1} \\ F_{comb_2} \\ F_{comb_3} \end{bmatrix} \sim \begin{bmatrix} V^2_{comb_1} \\ V^2_{comb_2} \\ V^2_{comb_3} \end{bmatrix} \quad \text{with} \quad i = [1, 2, 3] \tag{5.3}$$

The problem is solved using an IKM. Hence it was created (Paragraph 5.1), modelled (Paragraph 5.2), and simulated (Paragraph 5.3). Only the above described feed-forward control is used and no feedback control, because it is unknown if the platform position will be measured, and how that will be done. Moreover, it is not certain that the position of the platform can be measured accurately enough.

5.1 Inverse kinematic model

The rigid body model has four stiffnesses and hence four DOF per arm. The platform has only three DOF so a kinematic model would be underconstrained and an IKM would not have a unique solution. Additional force equations would be necessary to give a unique solution. However, a simple solution is to remove one DOF for the calculation of the IKM. The translation belonging to the longitudinal stiffness of the reinforced flexure should be removed, because it is by far the biggest stiffness in the model. It is in the order of 10^4 bigger than the lateral stiffness of the folded flexure, and in the order of 10^5 bigger than the lateral stiffness of the reinforced flexure.

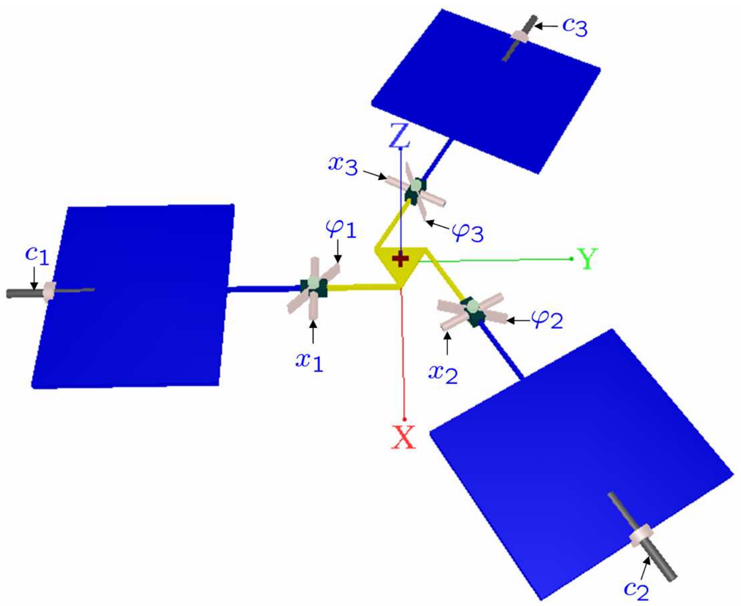

(a) Multibody model; the joints belonging to the longitudinal stiffnesses of the reinforced flexures are removed

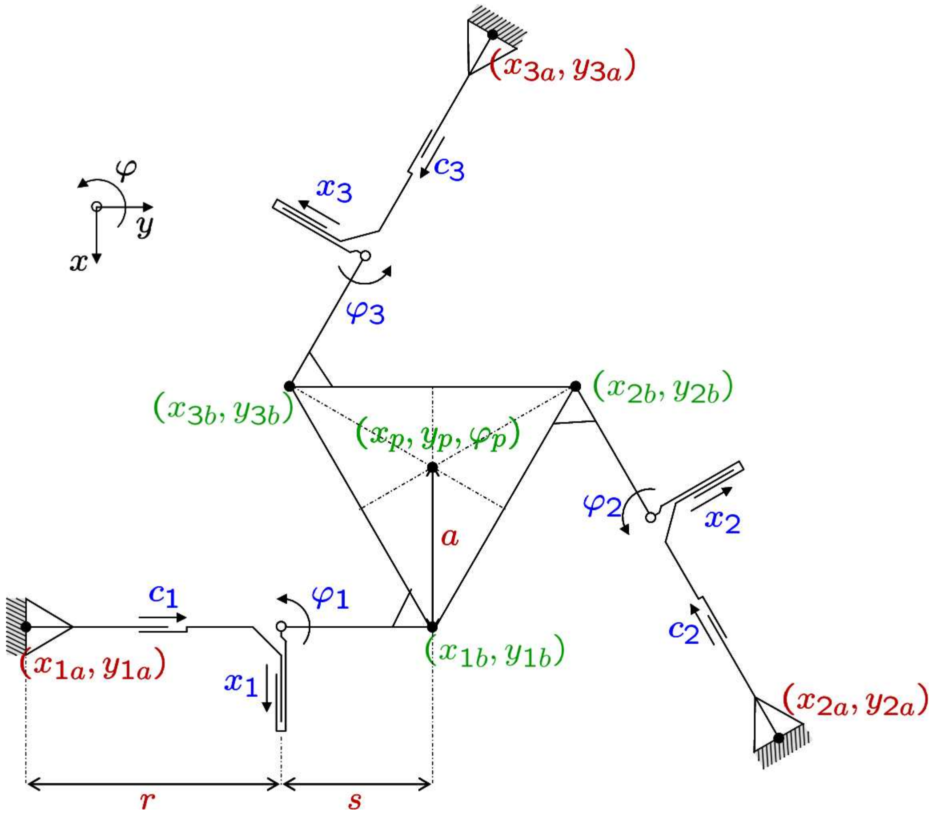

(b) Schematic represenation of above multibody model

Figure 5.1: Kinematic Model

Figure 5.1(b) shows a schematic figure of a kinematic model of the manipulator. No masses are taken into account and all springs are replaced by ideal joints, since a kinematic model does not contain any dynamics. The only movements that are possible are a translation due to the comb-drives (c_1, c_2, c_3) and a rotation and translation due to the leaf springs $(\varphi_1, \varphi_2, \varphi_3)$ and (x_1, x_2, x_3). The black dots only indicate the coordinates (e.g. (x_{1a}, y_{1a})). r, s and a are parameters. The coordinates at the corners of the platform can be written as functions of the platform coordinates:

$$x_{1b} = x_p + a\cos\varphi_p \qquad y_{1b} = y_p + a\sin\varphi_p \tag{5.4}$$
$$x_{2b} = x_p + a\cos\left(\varphi_p + \tfrac{2}{3}\pi\right) \qquad y_{2b} = y_p + a\sin\left(\varphi_p + \tfrac{2}{3}\pi\right) \tag{5.5}$$
$$x_{3b} = x_p + a\cos\left(\varphi_p + \tfrac{4}{3}\pi\right) \qquad y_{3b} = y_p + a\sin\left(\varphi_p + \tfrac{4}{3}\pi\right) \tag{5.6}$$

The following equation from arm_1 was made using Figure 5.1(b):

$$y_{1a} + r + c_1 + s\cos\varphi_1 = y_{1b} \tag{5.7}$$

Keeping in mind that:

$$\varphi_1 = \varphi_2 = \varphi_3 = \varphi_p \tag{5.8}$$

Rewriting Equation 5.7 delivers c_1 as a function of (x_p, y_p, φ_p):

$$c_1 = y_p + a\sin\varphi_p - s\cos\varphi_p - y_{1a} - r \tag{5.9}$$

Similar to arm_1, the following equations from arm_2 were made:

$$x_{2b} + s\cos\left(\varphi_2 + \tfrac{1}{6}\pi\right) + \tfrac{1}{2}x_2 + \tfrac{\sqrt{3}}{2}\left(c_2 + r\right) = x_{2a} \tag{5.10}$$
$$y_{2b} + s\sin\left(\varphi_2 + \tfrac{1}{6}\pi\right) - \tfrac{\sqrt{3}}{2}x_2 + \tfrac{1}{2}\left(c_2 + r\right) = y_{2a} \tag{5.11}$$

Now, two equations are needed instead of one, because the arm is not parallel to the x-axis or y-axis as arm 1 is. Both equations depend on the variable x_2, which can be eliminated by multiplying Equation 5.10 with $\sqrt{3}$ and adding Equation 5.11 to it. Rewriting the resulting equation delivers c_2 as a function of (x_p, y_p, φ_p):

$$\begin{aligned} c_2 = -\tfrac{\sqrt{3}}{2}\left(x_p - a\sin\left(\varphi_p + \tfrac{1}{6}\pi\right)\right) - \tfrac{\sqrt{3}}{2}s\cos\left(\varphi_p + \tfrac{1}{6}\pi\right) - \tfrac{1}{2}y_p \\ - \tfrac{1}{2}a\cos\left(\varphi_p + \tfrac{1}{6}\pi\right) - \tfrac{1}{2}s\sin\left(\varphi_p + \tfrac{1}{6}\pi\right) + \tfrac{\sqrt{3}}{2}x_{2a} + \tfrac{1}{2}y_{2a} - r \end{aligned} \tag{5.12}$$

Finally the equations from arm_3:

$$x_{3a} + \tfrac{\sqrt{3}}{2}\left(c_3 + r\right) - \tfrac{1}{2}x_3 + s\sin\left(\varphi_3 + \tfrac{1}{3}\pi\right) = x_{3b} \tag{5.13}$$
$$y_{3b} + s\cos\left(\varphi_3 + \tfrac{1}{3}\pi\right) + \tfrac{\sqrt{3}}{2}x_3 + \tfrac{1}{2}\left(c_3 + r\right) = y_{3a} \tag{5.14}$$

Multiplying Equation 5.13 with $\sqrt{3}$ and adding Equation 5.14 to it, eliminates x_3 and delivers c_3 as a function of (x_p, y_p, φ_p):

$$\begin{aligned} c_3 = \tfrac{\sqrt{3}}{2}\left(x_p - a\cos\left(\varphi_p + \tfrac{1}{3}\pi\right)\right) - \tfrac{\sqrt{3}}{2}s\sin\left(\varphi_p + \tfrac{1}{3}\pi\right) - \tfrac{1}{2}y_p \\ + \tfrac{1}{2}a\sin\left(\varphi_p + \tfrac{1}{3}\pi\right) - \tfrac{1}{2}s\cos\left(\varphi_p + \tfrac{1}{3}\pi\right) - \tfrac{\sqrt{3}}{2}x_{3a} + \tfrac{1}{2}y_{3a} - r \end{aligned} \tag{5.15}$$

Linearisation around zero of the IKM equations (5.9, 5.12 and 5.15) delivers the following transformation matrix (which is also given in [6], but with a different definition of a, a rotated coordinate system and a different matrix order):

$$\begin{bmatrix} c_1 \\ c_2 \\ c_3 \end{bmatrix} = \begin{bmatrix} \left.\frac{\partial c_1}{\partial \varphi_p}\right|_{\varphi_p=0} & \left.\frac{\partial c_1}{\partial x_p}\right|_{x_p=0} & \left.\frac{\partial c_1}{\partial y_p}\right|_{y_p=0} \\ \left.\frac{\partial c_2}{\partial \varphi_p}\right|_{\varphi_p=0} & \left.\frac{\partial c_2}{\partial x_p}\right|_{x_p=0} & \left.\frac{\partial c_2}{\partial y_p}\right|_{y_p=0} \\ \left.\frac{\partial c_3}{\partial \varphi_p}\right|_{\varphi_p=0} & \left.\frac{\partial c_3}{\partial x_p}\right|_{x_p=0} & \left.\frac{\partial c_3}{\partial y_p}\right|_{y_p=0} \end{bmatrix} \begin{bmatrix} \varphi_p \\ x_p \\ y_p \end{bmatrix}$$
$$\Leftrightarrow \begin{bmatrix} c_1 \\ c_2 \\ c_3 \end{bmatrix} = \begin{bmatrix} a & 0 & 1 \\ a & -\frac{\sqrt{3}}{2} & -\frac{1}{2} \\ a & \frac{\sqrt{3}}{2} & -\frac{1}{2} \end{bmatrix} \begin{bmatrix} \varphi_p \\ x_p \\ y_p \end{bmatrix} \tag{5.16}$$

The inverse of this matrix is:

$$\begin{bmatrix} \varphi_p \\ x_p \\ y_p \end{bmatrix} = \begin{bmatrix} \frac{1}{3a} & \frac{1}{3a} & \frac{1}{3a} \\ 0 & -\frac{\sqrt{3}}{3} & \frac{\sqrt{3}}{3} \\ \frac{2}{3} & -\frac{1}{3} & -\frac{1}{3} \end{bmatrix} \begin{bmatrix} c_1 \\ c_2 \\ c_3 \end{bmatrix} \tag{5.17}$$

These matrices give the global relation between comb-drive deflection and platform position.

5.2 20-sim model

Figure 5.2 shows the feed-forward position control 20-sim model. The IKM equations (Equations 5.9, 5.12 and 5.15) are put in the IKM submodel. A setpoint $(x_{p\_sp}, y_{p\_sp}, \varphi_{p\_sp})$ is input and the IKM will calculate the comb-drive deflections needed to ensure that the real platform position (x_p, y_p, φ_p) will follow the setpoint. The gains before and after the IKM, and the square root after the IKM reflect the proportionality between comb-drive deflection and voltage (Equation 5.3). The gains depend on the geometry, the stiffness of the system and the force-voltage relation of the comb-drives. If the platform position follows the setpoint in any case, the IKM works right.

As another check, the IKM equations are also put in submodel ‘Hp’. Instead of the setpoint, the real position of the platform is put in the IKM equations. The resulting comb-drive deflections should be very similar to the real comb-drive deflections, which are the states in the folded flexure submodels (‘Kff1’ to ‘Kff3’). Only a small deviation due to the neglected longitudinal stiffness is possible.

5.3 Simulation

5.3.1 Voltage-deflection relation

The model has been simulated for different setpoints in x and y-direction: $\{-12, -8, -4, 0, 4, 8, 12\}$ $[\mu\mathrm{m}]$ (see Figure 5.3), to be able to validate the model with measurements in Paragraph 6.1. Moreover, the effect of the IKM on the model is checked. Figure 5.3(a) shows the platform setpoint (x_{p_sp}, y_{p_sp}) as well as the platform deflection (x_p, y_p). Figure 5.3(b) shows the comb-drive voltages, calculated by the IKM. The comb-drive voltage squared, divided by the setpoint is a constant value for all setpoints, as can be seen in Figure 5.3(c). Hence, when the voltage squared is plotted against the deflection, a constant slope is visible. This means that, as expected, the voltage-deflection relation is quadratic (for small deflections), because the force-voltage relations of the comb-drives are quadratic, and the stiffnesses of the flexures are linear (for small deflections).

All possible slopes are calculated, except for the relation between comb-drive$_1$ and x_p, because the voltage of comb-drive$_1$ remains zero for movement in x-direction. The slope is not calculated for voltages

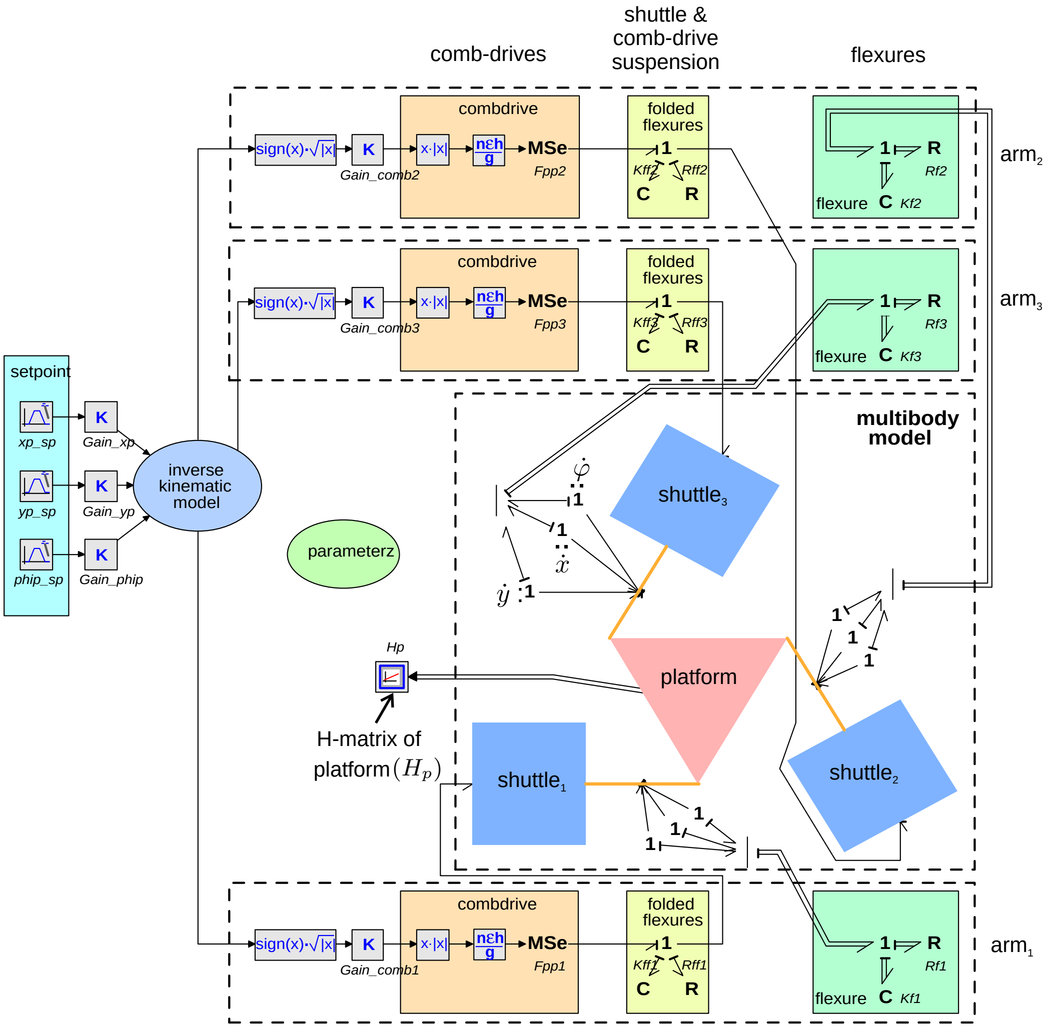

Figure 5.2: Feed-forward position control 20-sim model

lower than a certain minimum voltage, because the slope will go to infinity when the voltage is close to zero, which introduces spikes in the simulation. Moreover, the slope is only important when the setpoint is reached (i.e. $0.01 - 0.02$ and $0.035 - 0.045\,\mathrm{s}$).

The gains before and after the IKM are determined by trial and error. They are given in the table below:

parameter	**value**
gain_comb$_1$	19400
gain_comb$_2$	18900
gain_comb$_3$	18900
gain_φ_p	0.96
gain_x_p	0.735
gain_y_p	0.745

Table 5.1: Gain parameters

The ratio between $\frac{x_p}{V_{comb_3}^2}$ and $\frac{y_p}{V_{comb_1}^2}$ in the simulation is 0.81. If the flexures would have the same stiffness and the comb-drives the same strength, the ratio would be $\frac{\sqrt{3}}{2} \approx 0.866$, according to the matrix from Equation 5.17 (the factor belonging to x_p and c_3, divided by the factor belonging to y_p and c_1 is $\frac{\sqrt{3}}{2}$).

The same holds for the ratio between $\frac{y_p}{V_{comb_1}^2}$ and $\frac{y_p}{V_{comb_2}^2}$, which is 2.1 in the simulation. But if the flexures would have the same stiffness and the comb-drives the same strength, the ratio would be 2.0 (which is the factor belonging to y_p and c_1, divided by the factor belonging to y_p and c_2).

The model also has been simulated for different setpoints in φ-rotation: $\{-3, -2, -1, 0, 1, 2, 3\}$ $[°]$ (see Figure 5.4). Again, a constant slope returns from simulations, which means a quadratic relation exists between comb-drive voltage and platform rotation (for small rotations).

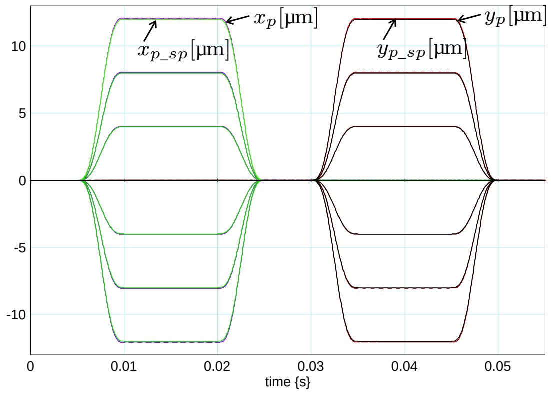

(a) Simulation with Platform setpoint (x_{p_sp}, y_{p_sp}) and platform deflection (x_p, y_p)

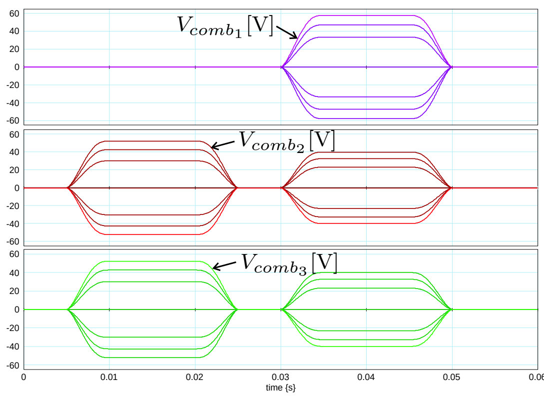

(b) Comb-drive voltages

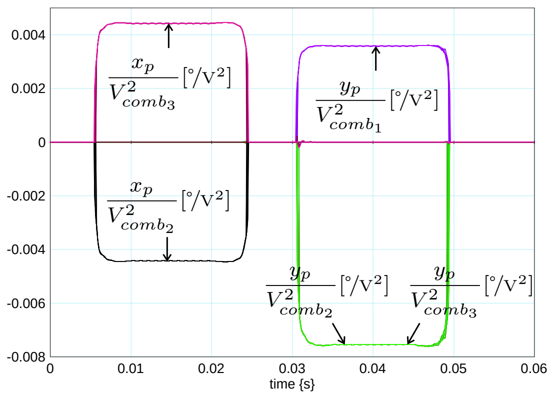

(c) Slope

Figure 5.3: Simulation for translational deflections

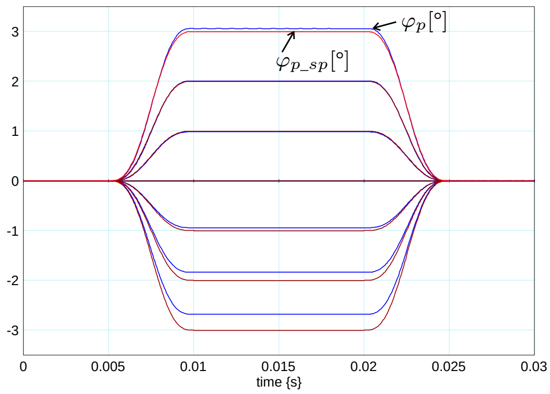

(a) Platform setpoint (φ_{p_sp}) and platform rotation (φ_p)

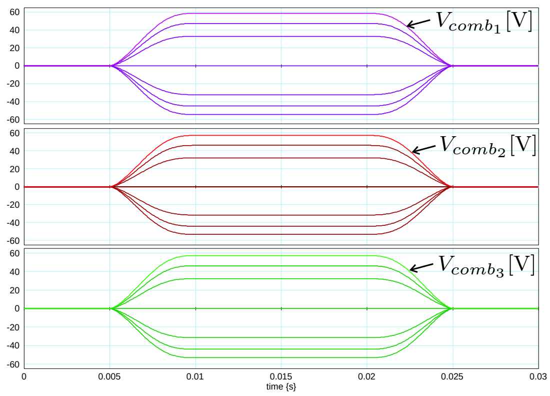

(b) Comb-drive voltages

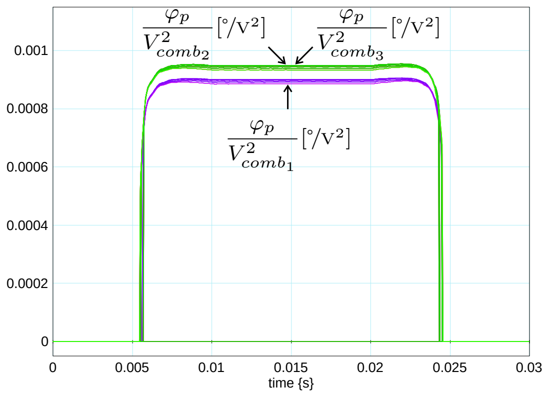

(c) Slope

Figure 5.4: Simulation for rotational deflection

Chapter 6

Measurements & Validation

6.1 Voltage-deflection relation

To verify the simulation from Paragraph 5.3.1, the platform deflection is measured for different comb-drive voltages. Voltages are applied in the ratio according to the simple linear kinematic model (see Equation 5.17), keeping in mind the square force-voltage relation of the comb-drives. For movement in the positive y-direction, the voltage on push comb-drive$_1$ is $\sqrt{2}$ times the voltage on pull comb-drive$_2$ and pull comb-drive$_3$. For movement in the positive x-direction, the voltage on comb-drive$_1$ is left zero; the voltage on pull comb-drive$_2$ and push comb-drive$_3$ is the same. The same holds for the negative directions, except that push and pull are switched.

Figure 6.1 shows the measured data points together with linear best-fit lines (using the Matlab function 'polyfit'), as well as the simulated data for the three platform coordinates. A negative voltage means a voltage on the pull comb-drive and a positive voltage means a voltage on the push comb-drive. In the x and y-direction the simulation and measurements match well. For the φ-rotation it matches less well. This is due to the fact that the real thickness of the flexures and comb-drive teeth is not known very accurately, so the real stiffness might be different, as well as the comb-drive strength. Especially because the stiffness depends on the thickness to the third power. Hence, a 5% deviance in thickness already becomes a 16% deviance in stiffness and this will also change the voltage-deflection relation.

For calculation of the best-fit line in x-direction, the measurements at $2500\,\mathrm{V}^2$ and $-2500\,\mathrm{V}^2$ were not taken into account, since the manipulator hit one or more end-stops. The difference between simulations and measurements are: in x-direction 2.3 %, in y-direction 3.9 % and in φ-rotation 12.8 %.

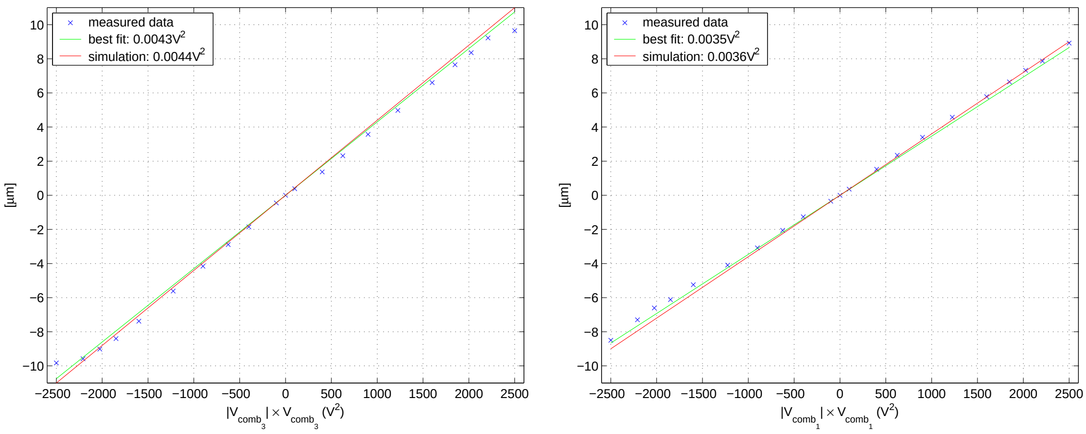

(a) x_p-$V_{comb_3}^2$ relation

(b) y_p-$V_{comb_1}^2$ relation

Figure 6.1: Voltage-deflection measurements, compared with simulation

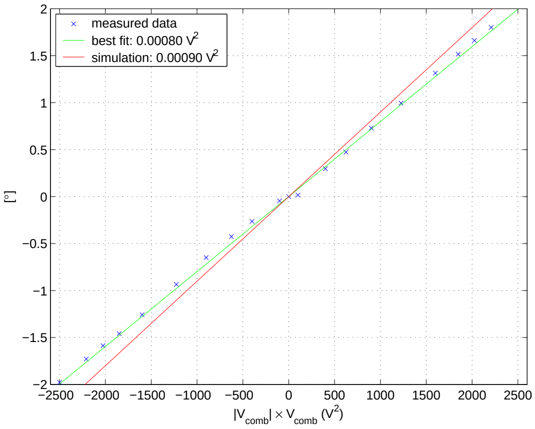

(c) φ-V_{comb} relation

Figure 6.1: Voltage-deflection measurements, compared with simulation

6.2 Resonance frequencies

In order to get more information about the manipulator, the resonance frequencies of the manipulator are measured. They were already simulated in Paragraph 4.4.2, so a comparison can be made. It gives different information than the voltage-deflection relation, since the resonance frequencies are influenced by masses and inertias, but not by the comb-drive strength. This is in contrast to the voltage-deflection relation, which is influenced by the comb-drive strength, but not by masses and inertias.

The resonance frequencies of the system were measured by putting a sinusoidal voltage with a fixed amplitude on the comb-drives and changing its frequency. The deflection of the platform is maximum at the resonance frequency. The system has very low damping, so the resonance frequency peak is very narrow. A 1-2 Hz change around the resonance frequency is even visible. Hence, visual inspection of the maximum deflection through an optical microscope works fine. The amplitude of the voltage should not be too small (otherwise vibrations would be invisible), nor too big (otherwise the system might hit an end-stop and damage). An amplitude of $14\,\mathrm{V}$ seemed to be a good compromise.

Each of the three platform coordinates has its own resonance frequency. Since the voltage can be put on the push comb-drives as well as the pull comb-drives, the measurements were done twice per coordinate: for the negative and positive direction. The measured resonance frequencies are compared with simulated resonance frequencies (from Table 4.2) in the table below:

coordinate	**measurements**		**model**	**difference**
	voltage freq. (Hz)	**force freq.** (Hz)	**freq.** (Hz)	
$+\varphi$	728 ± 2	1456 ± 4	1353 ± 10	7.1%
$-\varphi$	729 ± 2	1458 ± 4		
$+x$	581 ± 2	1162 ± 4	1122 ± 10	3.3%
$-x$	579 ± 2	1158 ± 4		
$+y$	600 ± 2	1200 ± 4	1163 ± 10	3.1%
$-y$	600 ± 2	1200 ± 4		

Table 6.1: Measured and simulated resonance frequencies

Because of the point-symmetry of the system, the resonance frequencies in all translational directions are expected to be the same. But the measurements show a deviation between the resonance frequencies in x and y direction, which is likely due to the following:

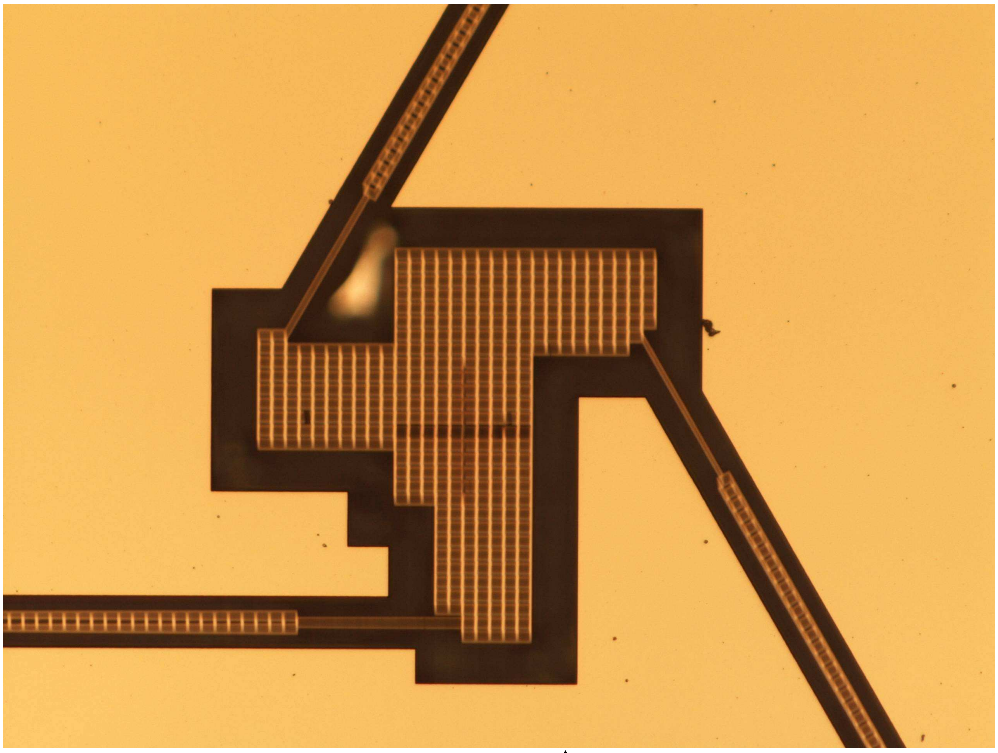

(a) x-direction $\updownarrow$

Figure 6.2: Pictures of the manipulator in resonance through an optical microscope

- Effects of the mask resolution were found, looking at the structure with a SEM (see Figure 6 in [6]).
- A difference exists in the Young's modulus between 30° or 60° structures and 0° or 90° structures.

The difference between simulated and measured resonance frequencies is likely to be caused by the following:

- The stiffness, masses and inertias were calculated and thus not known very accurately.
- When a sinusoidal voltage is applied on the comb-drives, the platform does not only vibrate in the actuated direction. This can be seen from the pictures taken at the resonance frequencies (see Figure 6.2). Especially in the y-direction, a deviation is visible on the top right hand side of the platform.
- The damping has a little influence on the resonance frequency. A higher damping will lower the resonance frequency a bit.

In the conclusions (Paragraph 7.1) more details are given.

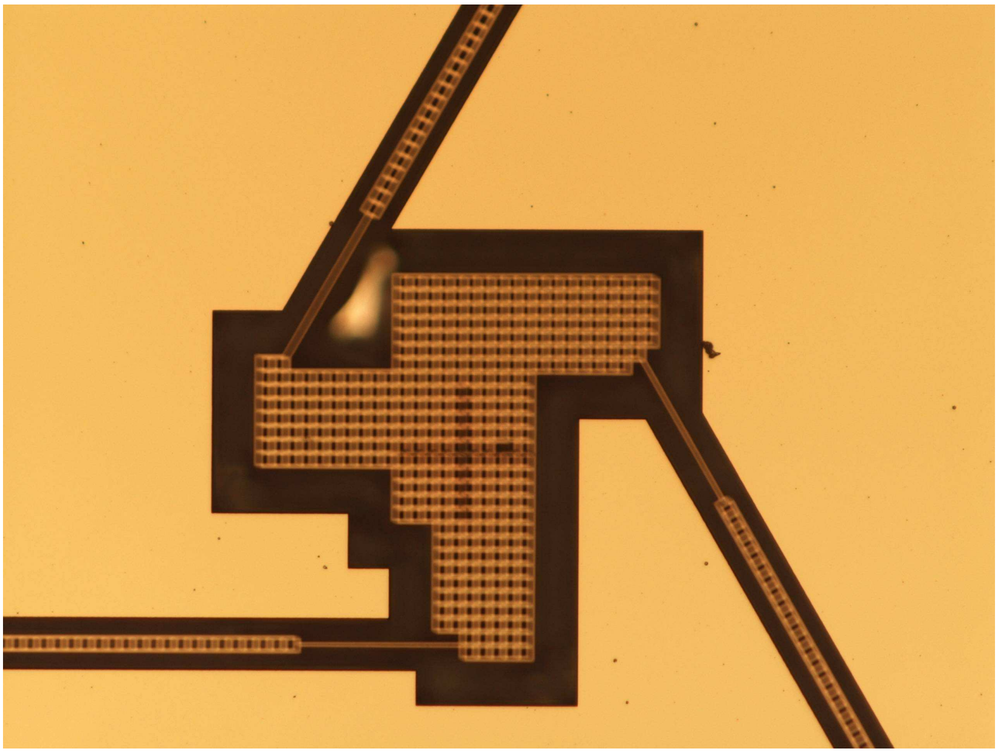

(b) y-direction $\longleftrightarrow$

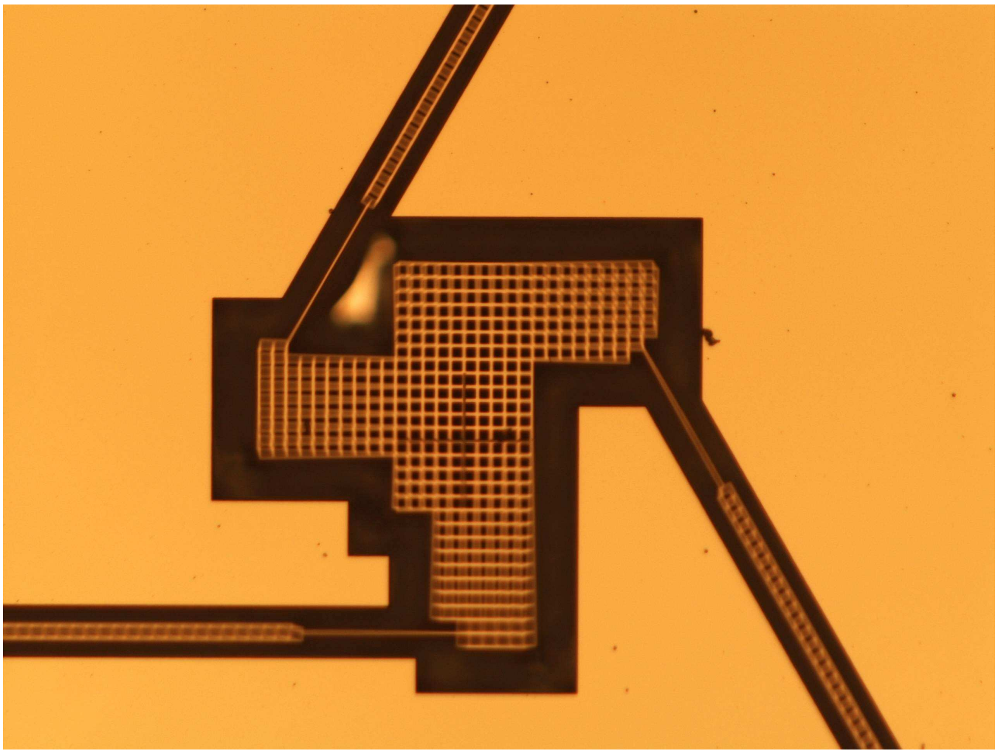

(c) φ-rotation ↺

Figure 6.2: Pictures of the manipulator in resonance through an optical microscope

Chapter 7

Conclusions & Recommendations

7.1 Conclusions

Body-editor

The body-editor of 20-sim is a great tool for creating 3D multibody models. Compared to modelling rigid bodies with 6-dimensional bond graphs, modelling with the body-editor is much easier, faster and less sensitive to mistakes. A kinematic construction of rigid bodies, which represents the manipulator's kinematic behaviour, was created in the body-editor. An equation model of the multibody model was generated and imported into 20-sim. Currently, flexible elements or springs cannot be modelled directly in the body-editor. Instead, it can be modelled in 20-sim and connected to the equation submodel of the multibody model. The way to model multidimensional springs should be connecting two rigid bodies with a stiffness, without using a construction of 1D-joints in the body-editor. However, some problems were encountered concerning this way of implementing a stiffness in 20-sim and its body-editor (drift in the spring position as well as numerical instabilities). Therefore a construction of 1D-joints was used for the flexures.

Validation

Validation showed that the behaviour of the modelled manipulator is close to the behaviour of the real manipulator. The simulated voltage-deflection relations of the manipulator match to the real voltage-deflection relation very well. The simulated resonance frequencies match to the measured resonance frequencies of the real manipulator, but the simulated resonance frequencies are a bit lower. Possible reasons for this deviation are:

- More material is etched away than designed, resulting in the mass being estimated too high. A lower mass in the model will increase the resonance frequencies, but has no effect on the voltage-deflection relation. When the holes are not $9 \times 9\,\mu\mathrm{m}$, but for example $9.4 \times 9.4\,\mu\mathrm{m}$ (which is a 9.1% increase in area), the mass decreases about 12% and the resonance frequency increases about 5.4%.

- The real stiffness is bigger than the modelled stiffness. A higher stiffness in the model will increase the resonance frequencies, but will also change the voltage-deflection relation. To maintain the voltage-deflection relation while increasing the stiffness, the comb-drive strength in the model should be increased as well. As mentioned before, the thickness of the flexures and comb-drive teeth is not known accurately enough, so the real stiffness might be different, as well as the comb-drive strength. Especially because the stiffness depends on the thickness to the third power. Hence, the voltage-deflection relation is very much affected by the thickness.

- The damping is not known very accurately. It is estimated roughly and assumed to be viscous.

7.2 Recommendations

Validation

More measurement data is necessary to improve the verification of the model. The voltage-deflection relation was only measured for specific voltages that will move the platform in the in-plane coordinates. For further measurements, certain voltages have to be applied on each comb-drive and the position of the platform has to be measured for all possible combinations of comb-drive voltages. This will result in a big table with much more information, because the position of the platform will also be measured for combined rotations and translations. Ideally, the measurements have to be performed for more than one device, to exclude measurement errors and to check whether a deviation exists between different manipulators. The measurement data can also be used for feed-forward control.

Modelling

The inverse kinematic model has to be implemented on the real manipulator to check whether it also works in reality. Probably a micro-controller can perform the calculations needed. In combination with the feed-forward control, a feedback control can be designed when is known what kind of measurement signals are to be expected. Different solutions can be thought of. To name a few:

- The position of the platform may be determined by measuring the capacitance in the comb-drives, which is related to the comb-drive deflection.
- A camera may monitor the position of the manipulator, which can be extracted with image-processing techniques.

When bigger translational or rotational deflections become possible in a future manipulator, better kinematics and dynamics are necessary in the model. For example the flexures need more accurate energy functions that are also valid for bigger deflections.

The out-of-plane manipulator has to be modelled to complete the model of the 6 DOF manipulator. When the out-of-plane manipulator and the 6 DOF manipulator are fabricated, measurements should be performed to validate the models.

Design

The design of the real manipulator was not intended to make it as compact and efficient as possible. Hence, the design of the real manipulator can be improved and optimised much, although criteria would be necessary. The model of the manipulator can be used to simulate and predict the behaviour of the manipulator for changes in the design.

- First of all, for use in a TEM, the size must be reduced. This can be accomplished by, for example, shifting the reinforced flexures inside the shuttle.
- Considering the size of the current shuttles, much more comb-drive teeth could be created, which will strengthen the manipulator and decrease the maximum voltage needed.
- Much space is wasted between platform and shuttles. This can be solved by shifting the flexures inside the shuttles. A nice consequence is that the size becomes smaller, while the performance is maintained.
- The size and position of the reinforcement in the flexures have to be considered. The advantage of reinforcement is that the longitudinal stiffness and the buckling force increase. But the disadvantage is that the lateral stiffness increases a bit, and the rotational stiffness increases much.

Appendix A

Homogeneous coordinates

A.1 Homogeneous matrices

The position p_i^0 of rigid body i with respect to the reference body in the planar case is (see Figure A.1):

$$p_i^0 = \begin{bmatrix} \varphi_i \\ x_i \\ y_i \end{bmatrix} \tag{A.1}$$

The position of a body can also be expressed in homogeneous coordinates. A homogeneous matrix H consists of a rotation matrix R and a position vector p. The rotation matrix was chosen such that a positive φ results in a counterclockwise rotation (to let clockwise be positive, R has to be transposed, but then many signs change). The position H_i^0 of body i with respect to the reference body is:

$$H_i^0 = \begin{bmatrix} R_i & p_i \\ 0 & 1 \end{bmatrix} = \begin{bmatrix} \cos(\varphi_i) & \sin(\varphi_i) & x_i \\ -\sin(\varphi_i) & \cos(\varphi_i) & y_i \\ 0 & 0 & 1 \end{bmatrix} \tag{A.2}$$

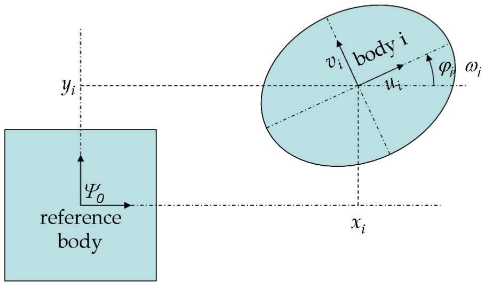

Figure A.1: Rigid body position

The position H_0^i of the reference body with respect to body i is the inverse of H_i^0. The inverse of a homogeneous matrix can simply be calculated with just transpositions:

$$\begin{aligned} H_0^i &= (H_i^0)^{-1} \\ &= \begin{bmatrix} R_i^T & -R_i^T p_i \\ 0 & 1 \end{bmatrix} \\ &= \begin{bmatrix} \cos(\varphi_i) & -\sin(\varphi_i) & -x_i\cos(\varphi_i) + y_i\sin(\varphi_i) \\ \sin(\varphi_i) & \cos(\varphi_i) & -x_i\sin(\varphi_i) - y_i\cos(\varphi_i) \\ 0 & 0 & 1 \end{bmatrix} \end{aligned} \tag{A.3}$$

A.2 Twists & wrenches

The generalized translational and angular speed in the 2- or 3-dimensional case is called a Twist (quantity T). And the generalized force and torque is called a Wrench (quantity W). Hence the mechanical power P is just: $P = W^T T$. For the twist $T_i^{i,0}$ of body i with respect to the reference body (expressed in body coordinates) holds:

$$T_i^{i,0} = \begin{bmatrix} \omega_i \\ u_i \\ v_i \end{bmatrix} = \begin{bmatrix} \dot{\varphi}_i \\ \dot{x}_i\cos(\varphi_i) - \dot{y}_i\sin(\varphi_i) \\ \dot{x}_i\sin(\varphi_i) + \dot{y}_i\cos(\varphi_i) \end{bmatrix} \tag{A.4}$$

For the wrench holds:

$$W = \begin{bmatrix} M \\ F_x \\ F_y \end{bmatrix} \tag{A.5}$$

So the power is:

$$P = W^T T = M\omega_i + F_x u_i + F_y v_i \tag{A.6}$$

Besides the column vector notation, a twist can also be written in 'tilde' notation. It is easier to be calculated in that way:

$$\begin{aligned} \tilde{T}_i^{i,0} &= H_0^i \dot{H}_i^0 \\ &= \begin{bmatrix} 0 & \dot{\varphi}_i & \dot{x}_i\cos(\varphi_i) - \dot{y}_i\sin(\varphi_i) \\ -\dot{\varphi}_i & 0 & \dot{x}_i\sin(\varphi_i) + \dot{y}_i\cos(\varphi_i) \\ 0 & 0 & 0 \end{bmatrix} \\ &= \begin{bmatrix} 0 & \omega_i & u_i \\ -\omega_i & 0 & v_i \\ 0 & 0 & 0 \end{bmatrix} \end{aligned} \tag{A.7}$$

For the twist of body i with respect to the reference body, but expressed in reference coordinates, holds:

$$\begin{aligned} \tilde{T}_i^{0,0} &= \dot{H}_i^0 H_0^i \\ &= \begin{bmatrix} 0 & \dot{\varphi}_i & -\dot{\varphi}_i y_i + \dot{x}_i \\ -\dot{\varphi}_i & 0 & \dot{\varphi}_i x_i + \dot{y}_i \\ 0 & 0 & 0 \end{bmatrix} \\ &= \begin{bmatrix} 0 & \omega_0 & u_0 \\ -\omega_0 & 0 & v_0 \\ 0 & 0 & 0 \end{bmatrix} \end{aligned} \tag{A.8}$$

Equations A.7 en A.8 imply a mapping of twists in different coordinate systems:

$$\begin{aligned} \tilde{T}_i^{i,0} &= H_0^i \dot{H}_i^0 \\ \Leftrightarrow (H_0^i)^{-1} \tilde{T}_i^{i,0} &= \dot{H}_i^0 \\ \Leftrightarrow \dot{H}_i^0 &= H_i^0 \tilde{T}_i^{i,0} \\ \tilde{T}_i^{0,0} &= \dot{H}_i^0 H_0^i \\ \Rightarrow \tilde{T}_i^{0,0} &= H_i^0 \tilde{T}_i^{i,0} H_0^i \end{aligned} \tag{A.9}$$

This mapping can also be written in column notation, with a so called ‘Adjoint’ representation of the H-matrix:

$$T_i^{0,0} = Ad_{H_i^0} T_i^{i,0} \tag{A.10}$$

With $Ad_{H_i^0}$:

$$Ad_{H_i^0} = \begin{bmatrix} 1 & 0 & 0 \\ -y_i & \cos(\varphi_i) & \sin(\varphi_i) \\ x_i & -\sin(\varphi_i) & \cos(\varphi_i) \end{bmatrix} \tag{A.11}$$

A twist is transformed according to Equation A.10. A wrench is similarly transformed in order to conserve power (P) and energy:

$$\left.\begin{aligned} T_i &= Ad_{H_c^i} T_c \\ W_c &= Ad_{H_c^i}^T W_i \end{aligned}\right\} \quad \begin{aligned} P &= W_i^T T_i \\ &= ((Ad_{H_c^i}^T)^{-1} W_c)^T Ad_{H_c^i} T_c \\ &= W_c^T Ad_{H_c^i}^{-1} Ad_{H_c^i} T_c \\ &= W_c^T T_c \end{aligned} \tag{A.12}$$

These transformations can be used to transform a stiffness matrix to other coordinates:

$$\begin{aligned} W_i &= K_i q_i \\ \Leftrightarrow W_i &= K_i Ad_{H_c^i} q_c \\ \Leftrightarrow (Ad_{H_c^i}^T)^{-1} W_c &= K_i Ad_{H_c^i}\, q_c \\ \Leftrightarrow W_c &= \underbrace{Ad_{H_c^i}^T K_i Ad_{H_c^i}}_{K_c}\, q_c \end{aligned} \tag{A.13}$$

And hence a stiffness matrix is transformed to other coordinates as follows:

$$K_c = Ad_{H_c^i}^T K_i Ad_{H_c^i} \tag{A.14}$$

Appendix B

Stiffness matrix transformations

B.1 Generalization of Newton's law to the planar case

A rigid body has three degrees of freedom in the planar case if there are no constraints: two translations (x, y) and a rotation (φ). In the one dimensional case, there is just one degree of freedom. See Figure B.1(a) for a schematic representation. Newton's second law for a point mass states:

$$F = \dot{p} \text{ , with } p = mv \tag{B.1}$$

Only when the mass is constant (i.e. $\dot{m} = 0$) it can be rewritten into:

$$F = m\dot{v} = m\ddot{x} \tag{B.2}$$

This can be generalized to the planar case:

$$W = J\dot{T} \tag{B.3}$$

$$\Leftrightarrow \begin{bmatrix} M \\ F_x \\ F_y \end{bmatrix} = J \begin{bmatrix} \ddot{\varphi} \\ \ddot{x} \\ \ddot{y} \end{bmatrix} \tag{B.4}$$

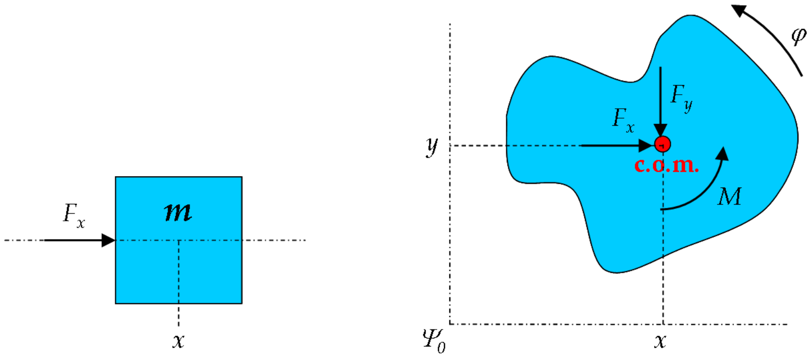

(a) One-dimensional case (b) Two-dimensional case

Figure B.1: Extension of a mass from 1D to 2D

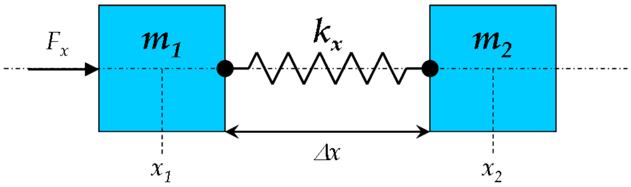

(a) One-dimensional case

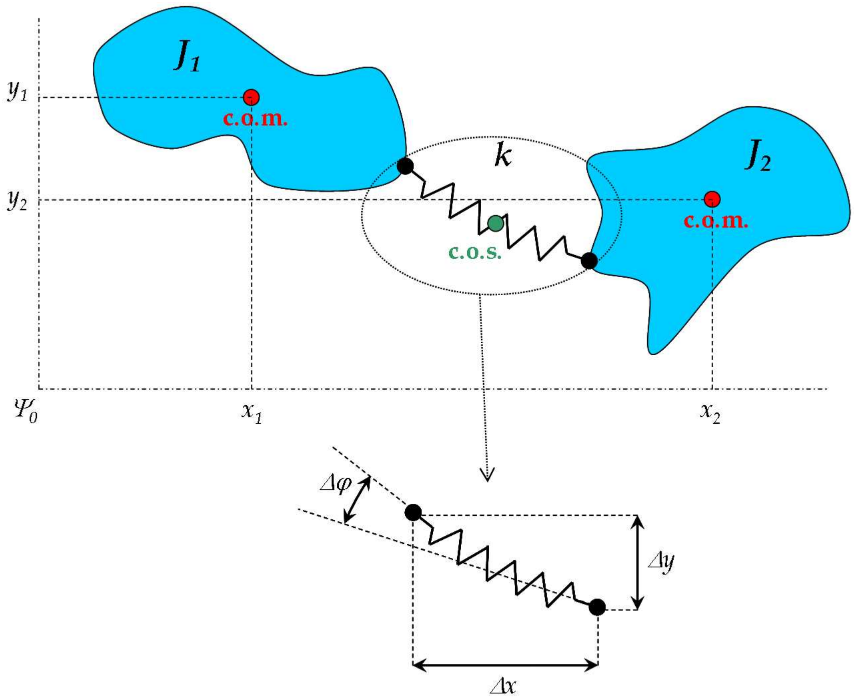

(b) Two-dimensional case

Figure B.2: Extension of a spring from 1D to 2D

With J a matrix that contains the mass and the mass moments of inertia of a rigid body with a random shape, described in its centre of mass (see Figure B.1(b) for a schematic representation.):

$$J = \begin{bmatrix} I & 0 & 0 \\ 0 & m & 0 \\ 0 & 0 & m \end{bmatrix} \tag{B.5}$$

The following equation describes a 1D linear spring:

$$F = kx \tag{B.6}$$

This can be extended to the planar case as well (see Figure B.2(b) for a schematic representation):

$$\begin{aligned} W &= Kq \\ \Leftrightarrow \begin{bmatrix} M \\ F_x \\ F_y \end{bmatrix} &= K \begin{bmatrix} \varphi \\ x \\ y \end{bmatrix} \end{aligned} \tag{B.7}$$

With K a stiffness matrix and q the generalized coordinates.

A rigid body is fully described by a mass and inertia matrix, and its 'centre of mass' (COM), despite its shape (see Equation B.5). Just like a rigid body has a COS, a spring consists of a certain point called 'centre of stiffness' (COS). When the spring is described in the COS, there is a minimum coupling between translation and rotation.

B.2 Theory for small deflections

A force and moment are acting on the end of the flexure in Figure B.3(a). Point 4 from the table at page 882 in [1] states that a force F_x that is acting on the end of a flexure (of length l, area moment of inertia I and Young's modulus E), results in an x-deflection and an angle φ of:

$$x = \frac{F_x l^3}{3EI} \qquad \varphi = -\frac{F_x l^2}{2EI} \tag{B.8}$$

The minus sign in the φ-F_x relation is due to the choice of the direction of the force and moment in the figure; a positive force will result in a negative rotation. Point 6 from the same table states that a torque M that is acting on the end of a flexure, results in a deflection x and an angle φ of:

$$x = -\frac{Ml^2}{2EI} \qquad \varphi = \frac{Ml}{EI} \tag{B.9}$$

The minus sign in the x-M relation is due to the choice of the direction of the force and moment in the figure; a positive moment will result in a negative x-deflection. When both a force and a torque are acting on the flexure, the deflections and angles from Equations B.8 and B.9 have to be superimposed. The equations can be rewritten in matrix notation as follows:

$$\begin{bmatrix} x \\ \varphi \end{bmatrix} = \begin{bmatrix} \dfrac{l^3}{3EI} & -\dfrac{l^2}{2EI} \\ -\dfrac{l^2}{2EI} & \dfrac{l}{EI} \end{bmatrix} \begin{bmatrix} F_x \\ M \end{bmatrix} \tag{B.10}$$

Inverting this matrix gives the relationship between the force versus displacement and torque versus angle of a flexure:

$$\begin{bmatrix} F_x \\ M \end{bmatrix} = \begin{bmatrix} 12\dfrac{EI}{l^3} & 6\dfrac{EI}{l^2} \\ 6\dfrac{EI}{l^2} & 4\dfrac{EI}{l} \end{bmatrix} \begin{bmatrix} x \\ \varphi \end{bmatrix} \tag{B.11}$$

Depending on the direction of the force and moment in the figure, the cross-terms of the stiffness matrix will either have a plus or minus sign.

The relationship between a force F_y and the y-deflection is derived from Hooke's law, which states there is a linear relationship between stress and strain: $\sigma = E\epsilon$. This can be rewritten as follows:

$$\begin{aligned} \sigma &= E\epsilon \\ \Leftrightarrow \frac{F_y}{A} &= E\frac{y}{l} \\ \Leftrightarrow F_y &= \frac{EA}{l}y \end{aligned} \tag{B.12}$$

Hence, the stiffness in the y-direction (k_y) is:

$$k_y = \frac{EA}{l} \tag{B.13}$$

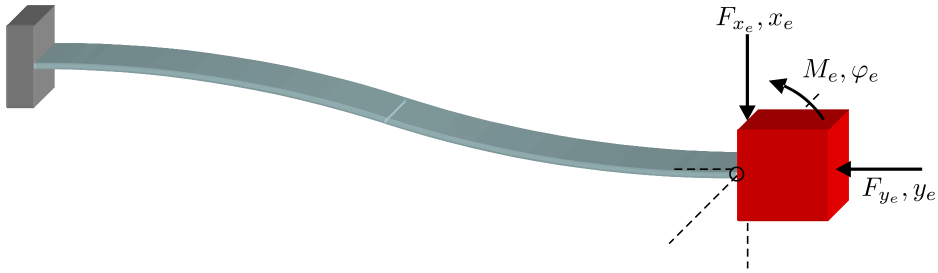

(a) Stiffness matrix described at the end

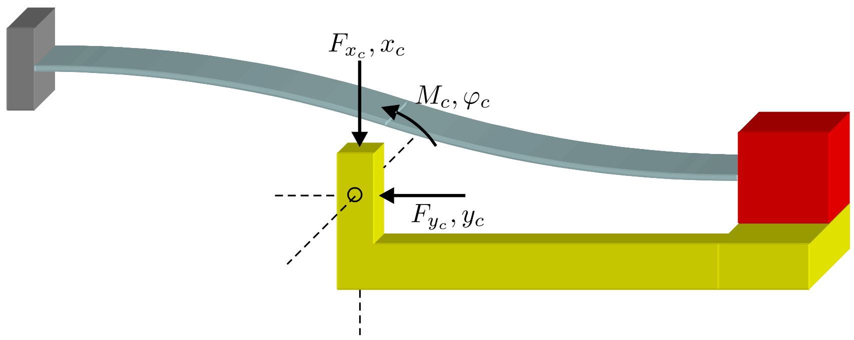

(b) Stiffness matrix described in the centre

Figure B.3: Flexure

The above stiffness k_y and the stiffness-matrix from Equation B.11 are combined in a 3×3 stiffness matrix:

$$K_e = \begin{bmatrix} 4\frac{EI}{l} & 6\frac{EI}{l^2} & 0 \\ 6\frac{EI}{l^2} & 12\frac{EI}{l^3} & 0 \\ 0 & 0 & \frac{EA}{l} \end{bmatrix} \tag{B.14}$$

This stiffness matrix is not described in the geometrical centre of the flexure, but at one of the ends. If a spring is described in the COS, there is maximum decoupling between rotational and translational stiffness. It seems obvious that the geometrical centre of the flexure coincides with the COS.

Figure B.3(b) shows a flexure with a force and moment acting on the centre of the flexure. A positive force on the end of the flexure will result in a negative moment on the centre of the flexure. The following equations relate the centre-forces to the end-forces and are rewritten to matrix-form:

$$\begin{cases} M_c = -\frac{1}{2}l \cdot F_{x_e} + M_e \\ F_{x_c} = F_{x_e} \\ F_{y_c} = F_{y_e} \end{cases} \Rightarrow \begin{bmatrix} M_c \\ F_{x_c} \\ F_{y_c} \end{bmatrix} = \begin{bmatrix} 1 & -\frac{1}{2}l & 0 \\ 0 & 1 & 0 \\ 0 & 0 & 1 \end{bmatrix} \begin{bmatrix} M_e \\ F_{x_e} \\ F_{y_e} \end{bmatrix} \tag{B.15}$$

The force-deflection relation can be rewritten as follows:

$$\begin{aligned} \begin{bmatrix} M_e \\ F_{x_e} \\ F_{y_e} \end{bmatrix} &= K_e \begin{bmatrix} \varphi \\ x_e \\ y_e \end{bmatrix} \\ \Leftrightarrow \begin{bmatrix} M_c \\ F_{x_c} \\ F_{y_c} \end{bmatrix} &= T K_e \begin{bmatrix} \varphi \\ x_e \\ y_e \end{bmatrix} \\ \Leftrightarrow \begin{bmatrix} M_c \\ F_{x_c} \\ F_{y_c} \end{bmatrix} &= \underbrace{T K_e T^T}_{K_c} \begin{bmatrix} \varphi \\ x_c \\ y_c \end{bmatrix} \end{aligned} \tag{B.16}$$

With T the transformation matrix from Equation B.15:

$$T = \begin{bmatrix} 1 & -\frac{1}{2}l & 0 \\ 0 & 1 & 0 \\ 0 & 0 & 1 \end{bmatrix} \tag{B.17}$$

So, the stiffness matrix K_c is:

$$K_c = T K_e T^T = \begin{bmatrix} \dfrac{EI}{l} & 0 & 0 \\ 0 & 12\dfrac{EI}{l^3} & 0 \\ 0 & 0 & \dfrac{EA}{l} \end{bmatrix} \tag{B.18}$$

The cross-terms are zero, which implies a maximum decoupling between the rotational stiffness and the translational stiffnesses. Hence, the centre of the spring is the COS. Advantages of describing the stiffness in the centre of the spring are:

- The direction of the forces and torque determine the sign of the cross-terms in K_e. Since these cross-terms are zero in K_c, the direction has no influence. Hence, no mistakes can be made whether the cross-terms need a plus or minus sign.
- Real flexures show shortening effects in the y-direction due to an x-deflection and rotation. When the flexure is described at the end of the spring, shortening effects of the flexure do not occur. But when the flexure is described at the centre of the spring, shortening effects do occur.
- Less computations are necessary when the flexure is simulated.

The transformation can also be calculated as follows. The stiffness is moved from the end of the leaf spring to the geometrical centre. This corresponds to a displacement of $\frac{1}{2}l$ in the y-direction. The homogeneous matrix H_c^i belonging to this transformation is:

$$H_c^i = \begin{bmatrix} 1 & 0 & 0 \\ 0 & 1 & \frac{1}{2}l \\ 0 & 0 & 1 \end{bmatrix} \tag{B.19}$$

The adjoint representation (see Equation A.11) of this homogeneous matrix is:

$$Ad_{H_c^i} = \begin{bmatrix} 1 & 0 & 0 \\ -\frac{1}{2}l & 1 & 0 \\ 0 & 0 & 1 \end{bmatrix} \tag{B.20}$$

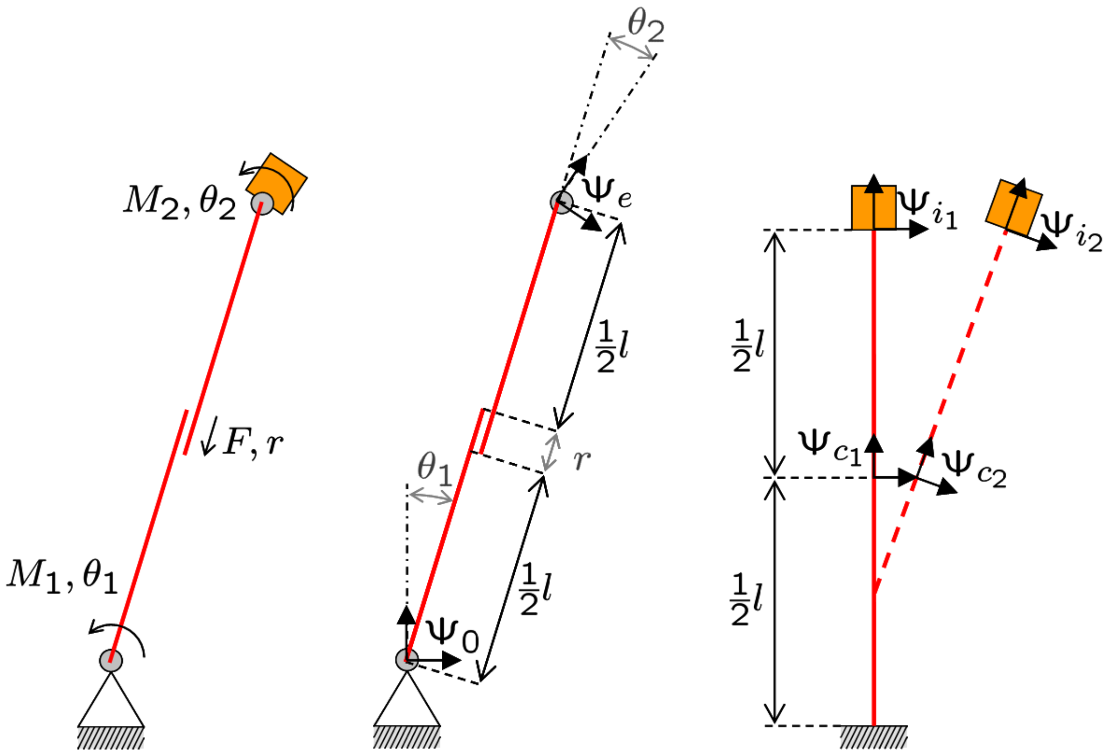

(a) Spacar leaf spring (b) Spacar leaf spring (c) Multibody leaf spring

Figure B.4: Coordinate transformation for Spacar leaf spring and a multibody leaf spring

B.3 Spacar leaf spring

In the Finite Element program Spacar, different coordinates and a different stiffness matrix is used for a leaf spring (see Figure B.4(a)). It will be shown that this is an awkward way of representation from a multibody point of view. In fact a mechanical construction is used to obtain similar behaviour. This construction consists of a translational spring that is connected to torsion springs on both sides through (massless) rods. In Sections B.3.1 and B.3.2 the equivalent stiffness matrices at the end of the leaf springs will be calculated for both ways of modelling. The leaf spring equation in Spacar is:

$$\begin{bmatrix} F \\ M_1 \\ M_2 \end{bmatrix} = K_s \begin{bmatrix} r \\ \theta_1 \\ \theta_2 \end{bmatrix} \tag{B.21}$$

With K_s:

$$K_s = \begin{bmatrix} \frac{EA}{l} & 0 & 0 \\ 0 & 4\frac{EI}{l} & -2\frac{EI}{l} \\ 0 & -2\frac{EI}{l} & 4\frac{EI}{l} \end{bmatrix} \tag{B.22}$$

B.3.1 Leaf spring model from a multibody point of view

The jacobian J_{mb} describes a mapping of twists from T_c to T_i, which can be used to transform the stiffness matrix from the centre of the spring (which is assigned to Ψ_c) to the end of the spring (which is assigned to

Ψ_i). See Figure B.4(c).

$$T_i = J_{mb}\,(\varphi_c, x_c, y_c)\,T_c \tag{B.23}$$

The distance between Ψ_{i_1} and Ψ_{i_2} (φ_i, x_i, y_i) is related to the distance between Ψ_{c_1} and Ψ_{c_2} (φ_c, x_c, y_c) as follows:

$$\begin{aligned} \varphi_i &= \varphi_c \\ x_i &= x_c + \tfrac{1}{2} l \sin(\varphi_c) \\ y_i &= y_c + \tfrac{1}{2} l \end{aligned} \tag{B.24}$$

Differentiating these equations to time and putting them in matrix form delivers the jacobian J_{mb}:

$$\begin{bmatrix} \dot{\varphi_i} \\ \dot{x_i} \\ \dot{y_i} \end{bmatrix} = \begin{bmatrix} 1 & 0 & 0 \\ \frac{1}{2} l \cos(\varphi_c) & 1 & 0 \\ 0 & 0 & 1 \end{bmatrix} \begin{bmatrix} \dot{\varphi_c} \\ \dot{x_c} \\ \dot{y_c} \end{bmatrix} \tag{B.25}$$

For small rotations $\cos(\varphi_c) = 1$ and hence J_{mb} becomes:

$$J_{mb} = \begin{bmatrix} 1 & 0 & 0 \\ \frac{1}{2} l & 1 & 0 \\ 0 & 0 & 1 \end{bmatrix} \tag{B.26}$$

The stiffness matrix from Equation B.18 can be transformed with this jacobian, because the relation between W_c and q_c can be rewritten as follows:

$$\begin{aligned} & W_c = K_c\, q_c \\ \Leftrightarrow\ & W_c = K_c J_{mb}^{-1}\, q_i \\ \Leftrightarrow\ & W_i = (J_{mb}^{-1})^T K_c J_{mb}^{-1}\, q_i \end{aligned} \tag{B.27}$$

Hence:

$$K_i = (J_{mb}^{-1})^T K_c J_{mb}^{-1} = \begin{bmatrix} 4\dfrac{EI}{l} & -6\dfrac{EI}{l^2} & 0 \\ -6\dfrac{EI}{l^2} & 12\dfrac{EI}{l^3} & 0 \\ 0 & 0 & \dfrac{EA}{l} \end{bmatrix} \tag{B.28}$$

And this is the equivalent stiffness at the end of the spring again, as computed in Section B.2.

B.3.2 Spacar leaf spring model

The jacobian J_{sp} describes a mapping from the three coordinates that Spacar uses (i.e. r, θ_1 and θ_2) to a twist T_e. See Figure B.4(b).

$$T_e = J_{sp}\,(r, \theta_1, \theta_2) \begin{bmatrix} \dot{r} \\ \dot{\theta}_1 \\ \dot{\theta}_2 \end{bmatrix} \tag{B.29}$$

J_{sp} is computed in the same way as in Paragraph B.3.1, by first computing φ_e, x_e and y_e as functions of r, θ_1 and θ_2:

$$\begin{aligned} \varphi_e &= \theta_1 + \theta_2 \\ x_e &= x_0 + (l + r)\sin(\theta_1) \\ y_e &= y_0 + (l + r)\cos(\theta_1) \end{aligned} \tag{B.30}$$

Differentiating these equations to time and putting them in matrix form delivers the jacobian:

$$\begin{bmatrix} \dot{\varphi}_e \\ \dot{x}_e \\ \dot{y}_e \end{bmatrix} = \begin{bmatrix} 0 & 1 & 1 \\ \sin(\theta_1) & (l+r)\cos(\theta_1) & 0 \\ \cos(\theta_1) & -(l+r)\sin(\theta_1) & 0 \end{bmatrix} \begin{bmatrix} \dot{r} \\ \dot{\theta}_1 \\ \dot{\theta}_2 \end{bmatrix} \tag{B.31}$$

By using the stiffness matrix from Equation B.22, K_{s_2} is computed as follows:

$$K_{s_2} = (J_{sp}^{-1})^T K_s J_{sp}^{-1} \tag{B.32}$$

K_{s_2} is full of sines and cosines. But for small rotations and translations: $\cos(\varphi_c) = 1$, $\sin(\varphi_c) = 0$ and $r \ll l$. Then, K_{s_2} becomes:

$$K_{s_2} = \begin{bmatrix} 4\dfrac{EI}{l} & -6\dfrac{EI}{l^2} & 0 \\ -6\dfrac{EI}{l^2} & 12\dfrac{EI}{l^3} & 0 \\ 0 & 0 & \dfrac{EA}{l} \end{bmatrix} \tag{B.33}$$

Since the equivalent stiffness matrices at the end of the leaf spring are the same for both models (see Equations B.28 and B.33), the models are equivalent and show the same behaviour. However, the multibody model is preferred, because for the Spacar model, a mechanical construction is needed. Another advantage is that the stiffness matrix has no cross terms. Hence, the multibody model is simpler and needs less computations.

Bibliography

[1] J.M. Gere and S.P. Timoshenko, “Mechanics of Materials”, *Stanley Thornes (Publishers) Ltd*, Fourth SI edition, United Kingdom, 1999

[2] Rob Legtenberg, “Electrostatic actuators fabricated by surface micromachining techniques”, *Ph.D. thesis, University of Twente*, The Netherlands, 1996

[3] Ville Kaajakari, “Silicon as an anisotropic mechanical material”, `http://www.kaajakari.net/~ville/research/tutorials/elasticity_tutorial.pdf`, Finland, 2003

[4] Jan van Eijk, “On the design of plate-spring mechanisms”, *Ph.D. thesis, University of Delft*, The Netherlands, 1985

[5] B.R. de Jong et al., “Nanometer resolution TEM sample manipulator for rotational and translational positioning”, *Eurosensors 2005, TP43*, Barcelona, Spain

[6] B.R. de Jong et al., “A planar 3 DOF sample manipulator for nano-scale characterization”, *MEMS 2006*, Istanbul, Turkey

[7] H.M.J.R. Soemers, “Flexures”, *Pre-release*, Enschede, The Netherlands, 2006

[8] M.P. Koster, “Constructieprincipes voor het nauwkeurig bewegen en positioneren”, *Twente University Press*, Enschede, The Netherlands, 1996

[9] David Elata and Vitaly Leus, “How slender can comb-drive fingers be?”, *J. Micromech. Microeng.* ***15*** *(2005), 1055–1059*